

Contents lists available at ScienceDirect

Combustion and Flame

journal homepage: www.elsevier.com/locate/combustflame



Soot-based Global Pathway Analysis: Soot formation and evolution at elevated pressures in co-flow diffusion flames



Dezhi Zhou, Suo Yang*

Department of Mechanical Engineering, University of Minnesota-Twin Cities, Minneapolis, MN 55455, USA

ARTICLE INFO

Article history: Received 23 September 2020 Revised 2 January 2021 Accepted 3 January 2021

Keywords: Soot Elevated pressure Chemical kinetics Soot-based Global Pathway Analysis (SGPA)

ABSTRACT

One of the major concerns in high pressure combustion is its high soot yield. An exact and comprehensive mechanism behind this phenomenon, from a chemical kinetics perspective, is still elusive. In this study, a series of pressurized (1-16 atm) co-flow ethylene diffusion sooting flames are simulated with detailed finite-rate chemistry and molecular transport. The experimental maximum soot volume fraction and its scaling law with pressure are well reproduced by the simulations. To extract kinetic information from the complex sooting reacting system, a Soot-based Global Pathway Analysis (SGPA) method is developed to identify the dominant Global Pathways (GPs) from fuel to soot by considering carbon element flux from gaseous species to soot. Using SGPA, the dominance and sensitivity of soot chemical pathways at elevated pressures are revealed. It is found that increasing pressure shifts the first ring Polycyclic Aromatic Hydrocarbon (PAH) formation from C₃H₃ recombination to reactions involving C₂H₂. At 1 atm, the production of C₂H₂ for surface growth is purely controlled by the H-abstraction of C₂H₄ and C₂H₃. In contrast, at elevated pressures, the production of C₂H₂ for surface growth is also influenced by many other reactions including some third body reactions. The SGPA method reveals that the mismatch of predicted PAH with the experimental data at 12 atm is majorly caused by the rate coefficient uncertainty of the reaction $C_2H_2 + A1CH_2 = C_9H_8 + H$. Based on the analysis by SGPA, the mechanism reduction based on Directed Relation Graph with Error Propagation (DRGEP) with A2 and C2H2 as the target species deleted significant species such as C_9H_8 , C_9H_7 , incurring inaccurate soot field prediction. It is also found that the combined dominance of GPs with heavier PAH species (A4-A7) is even greater than the most dominant GP at the flame wing regions, indicating that heavier PAH species play critical roles for soot nucleation and condensation, especially at the flame wing regions.

© 2021 The Combustion Institute. Published by Elsevier Inc. All rights reserved.

1. Introduction

Practical engine combustors all operates at elevated pressures to achieve high efficiency and compact sizes [1]. In recent years, the concept of supercritical carbon dioxide (sCO₂) power cycles, featuring high thermal efficiency and almost 100% carbon capture, attracts significant attention but operates at even higher pressures (e.g., 100–300 bar). The increased pressures in combustion lead to one major concern: high soot yield. The high soot yield under elevated pressures was observed and investigated in many laminar sooting flame experiments [2–5]. Most of the experimental studies attribute this phenomenon to higher temperature, steeper soot precursor concentration gradients, and increased gas density. Specifically, the maximum soot volume fraction in flames increases with pressure, with the dependence of soot on pressure

E-mail address: suo-yang@umn.edu (S. Yang).

becoming weaker as pressure is further increased (i.e., the trend is saturated).

To study the underlying physics of soot formation and evolution under elevated pressures, numerical studies have been conducted for pressurized laminar flames, such as the C2H4-fueled pressurized flames in the International Sooting Flame workshop 4 (ISF-4), including the Target Flame (TF) 2 (laminar pressurized diffusion flames with pressure range from 1 to 16 atm) [6-8], TF3 (laminar premixed pressurized flames with pressure range from 0.1-3.0 MPa) [9], and TF4 (laminar premixed pressurized flames with pressure range from 0.1-0.5 MPa) [10]. One of the earliest simulation works for TF2 is conducted by Burali et al. [11], who simulated TF2 with the purpose of assessing the accuracy of constant Lewis number in laminar flame simulations. Abdelgadir et al. [12] conducted another simulation work on TF2 with pressure range from 1 atm to 8 atm, focusing on the effects of hydrodynamics and mixing on soot formation and growth at elevated pressures, specifically, the sensitivity of soot precursors to mixture fraction scalar dissipation rate. As reported by Liu et al. [13],

^{*} Corresponding author.

the flame downstream centerline velocity remains approximately unchanged with the increased pressures, due to the effect of lower jet velocity (to keep the same mass flow rate) but narrower flame cross-sectional area (due to the enhanced buoyancy effect under elevated pressures). Abdelgadir et al. [12] showed that the scalar dissipation rate field changes regardless the almost unchanged velocity, leading to important modifications to the concentrations of the soot precursors and, in turn, to the soot yield. They concluded that the variation of scalar dissipation rate across the pressurized flames is the key to interpreting the experimentally observed trends with increasing pressure. Another numerical study by Eaves et al. [14] on TF3 (at pressures from 2 to 15 atm) reveals another mechanism of high soot yield with increasing pressure. They found that the elevated pressures can increase the rates of soot nucleation, condensation, and surface growth. After initiation by the increased gas density, the condensation and surface growth rates increase due to the elevated Polycyclic Aromatic Hydrocarbon (PAH) and C₂H₂ molar concentrations. As a result, the increased soot surface area in turn allows for higher condensation and surface growth rates. Hence, a positive feedback loop is formed and soot formation is enhanced sharply with elevated pressures. In a following work, Eaves et al. [15] found that for pressures above 20 atm, PAH condensation instead of surface growth is the dominant mechanism on the flame wings.

Specifically for co-flow diffusion sooting flames, Gulder and his coworkers [3,16–19] has extensively built a experimental database at different pressure ranges for different fuels. The work in Ref. [16] experimentally studies the laminar non-premixed methane-air flames over the pressure range from 0.5 to 4 MPa. One simulation work of this methane-air flame was conducted by Liu et al. [13]. They showed that in the pressure range of 20 - 40 atm, both simulation and experiment exhibit a diminishing sensitivity of soot propensity to pressure. The decrease of the predicted sensitivity of soot to pressure is much greater than experimentally observed. Another numerical study on the n-heptane flame [17] at pressures of 1 10 atm [20] showed that the soot formation processes are enhanced with increasing pressure. In addition, PAH condensation is the soot evolution process most sensitive to pressure.

With these numerical investigations of pressurized laminar sooting flames, different aspects are accounted for the mechanism of increasing soot yield with increasing pressure. First of all, it is seen that in co-flow diffusion flames, the pressure effect on the flame shape due to buoyancy decreases the flame cross-section area. However, the flame centerline velocity and flame height barely change across the set of flames with different pressures (and thus the sooting zone, which is fuel-rich and hot, also barely changes), indicating that the main reason of soot yield increase is not due to the change of residence time. In addition, other effects such as the increased mixture density and varied scalar dissipation rate caused by increasing pressure are also discussed. However, as pointed out by Karatacs et al. [1], the chemical kinetic effects on soot precursors formation with increasing pressure is significant, due to the existence of third body reactions and other pressure dependent reactions. However, there is no comprehensive work to investigate the pressure effects on the detailed finite-rate chemistry and how the change of reaction pathways alter the formation and evolution of soot.

For this reason, more detailed numerical analysis needs to be conducted to obtain fundamental understanding on the chemical kinetics of soot formation and evolution at elevated pressures. However, realistic chemical mechanisms describing the combustion and PAH formation typically involve hundreds of species and thousands of reactions [21,22]. Due to their large sizes and complicated coupled relations, it remains a formidable task to extract kinetic insights from the reacting systems. To the best knowledge

of the authors, the pressure effect on chemical kinetics of PAH and soot formation in pressurized laminar flames is only mentioned by Liu et al. [13], which only select the reactions that form benzene for comparison to investigate pressure effect on these benzene-forming reactions. They showed that the first ring PAH species formation (e.g., benzene) by acetylene and n-butadienyl becomes more significant with the increased pressures. In this sense, systematic diagnostic tools are necessary to obtain useful information. In the past few years, Gao, Yang, and Sun developed Global Pathway Analysis (GPA) [23-25], a hierarchical framework to automatically and quantitatively analyze reacting systems. GPA identifies important global pathways (GPs), which are the reaction pathways from a user-defined start species to a user-defined end species, based on atomic carbon flux analysis. GPA algorithm is much more powerful than traditional (manual) flux analysis because it can automatically extract species and reaction relations in multi-dimensional reacting flow simulations with detailed chemistry. In addition, compared with the algorithms such as Directed Relation Graph (DRG) [26] which could underestimate the importance of certain species due to their small flux and lead to broken pathways, GPA can well identify the GPs with these important species with small flux but large combined flux. GPA has been successfully applied to study both laminar flames [25] and turbulent flames [24]. In this study, a new soot-based GPA (SGPA) is developed and applied to understand the complex chemical kinetics for the sooting process and their pressure dependence.

To sum up, there are three primary objectives in this study. First of all, a systematic way to analyze detailed chemical kinetics in sooting flames (i.e., SGPA) is developed. Secondly, a series of pressurized co-flow diffusion flames from 1 to 16 atm are simulated. With the newly developed SGPA, the dominant reaction pathways from fuel to soot are identified at different pressures, revealing the pressure effects on the PAH formation and growth, soot nucleation, condensation and surface growth. Thirdly, based on SGPA, several deficiencies of the PAH formation reactions in the existing detailed and reduced chemical mechanisms are found, so that these mechanisms can be improved for future simulation of pressurized sooting flames.

The remaining paper is structured as follows. The details of sooting flame modeling and the development of SGPA are presented in Section 2. In Section 3, a series of pressurized laminar diffusion sooting flames are simulated, and SGPA are conducted to illustrate the dominant kinetic pathways in sooting flames. Conclusions are presented in Section 4.

2. Numerical modeling and analysis methodology

2.1. Transport equations and numerical schemes

In this study, the transport equations of gas-phase species, momentum and energy are solved with NGA [27], a finite difference code for low-Mach number laminar and turbulent reacting flows. Constant Lewis numbers, generated from 1-D flamelet solutions, are used for species diffusion coefficient calculations. The validity of constant Lewis numbers method in laminar flames was verified by Burali et al. [11]. Soret and Dufour effects are neglected for gasphase species [28]. To numerically solve these transport equations, a third-order WENO scheme [29] is used for the convection terms in the scalar equations. A second-order finite difference centered scheme is employed for diffusion terms in the scalar equations and the convection/diffusion terms in the momentum equation. In this study, radiation is accounted by adding a source term to the energy equation, based on the RADCAL model of Barlow et al. [30]. Four greenhouse gas-phase species (CO2, H2O, CH4 and CO) are considered for the radiative heat losses. Soot particle radiation is calculated by the optically thin model [31], due to the relatively

low soot concentration in these types of diffusion flames (maximally around 6 ppm at 16 atm in this study). It is reported by Liu et al. [32] that the optically thin model in these types of laminar sooting flames with about 1 ppm soot (the same order of magnitude as the soot volume fraction in our study) showed less than 6% discrepancy in terms of soot prediction.

2.2. Soot modeling

For soot modeling, a bivariate parameterization (volume V and surface area S) of the Number Density Function (NDF) [33] is used. For high dimensional (i.e., 2D/3D) simulations, the Method of Moments (MOM) is a computationally tractable technique. In this approach, instead of directly solving for the NDF of the soot population [34], MOM solves for the statistical moments $M_{X,y}$ of the NDF. With the bivariate description, joint moments of the NDF are given by

$$M_{x,y} = \sum_{s=0}^{\infty} V_s^x S_s^y N_s, \tag{1}$$

where the summation over s implies summation over the entire bivariate state space and N_s is the number density of particles with volume V_s and surface area S_s . The subscripts x and y denote the order of the moment in volume and surface area, respectively. Specifically, $M_{0.0}$ represents the total number density, $M_{1.0}$ represents the total volume fraction, and $M_{0,1}$ represents the total surface area. However, MOM faces the problem of closure: evaluation of the source term $\dot{M}_{x,y}$ depends on moments that are not directly solved for, which requires further modeling. In this study, the closure is obtained with the Hybrid Method of Moments (HMOM) [33], which explicitly accounts for the bimodality of the soot NDF by including an additional transport equation for a delta function representing the number density of incipient soot particles N_0 . As experimentally observed in Ref. [8], the soot size distribution is not changing much with the increasing pressure, which justified the usage of HMOM at elevated pressures. In this model, nucleation, condensation, coagulation, surface growth, oxidation, and oxidation-induced fragmentation are included. This model has been widely validated in laminar sooting flames [33,35,36]. Characterized by high Schmidt number, the diffusion for soot particles are neglected. Thermophoresis, however, is found to be important in sooting flames [37], thus considered in this study.

2.3. Chemical kinetics

The chemical mechanism used in this study is based on the mechanism developed by Blanquart et al. [21], which encompasses the high temperature combustion of fuels from methane to isooctane and places emphasis on the formation of soot precursors up to cyclopenta[cd]pyrene (A4R5), including the PAH species that contribute to dimer formation: naphthalene (A2), acephenanthrene (A2R5), biphenyl (P2), phenanthrene (A3), acephenanthrene (A3R5), pyrene (A4), fluoranthene (FLTN) and A4R5. The light PAH species (e.g., A2 and A2R5) are also included as soot precursors for dimerization in this study, because it is reported by Frenklach and Mebel [38] that A2 and A2R5 can undergo bridge-forming reactions to form dimers. The mechanism of Narayanaswamy et al. [22] expands this base mechanism to model the high-temperature oxidation of aromatic species. The final mechanism contains 158 species and 1804 reactions and is used in this study (named as NBP mechanism hereafter). To show the mechanism reduction effect on soot formation in pressurised flames, a reduced NBP mechanism [37] is also used, which contains 47 species and 290 reactions (named as RNBP hereafter). Due to the reduction, the PAH precursor contributing to dimers only include A2 in RNBP.

We also considered a more detailed mechanism developed by Selvaraj et al. [39], which contains PAH precursors with higher aromatic rings than A4R5, including chrysene, benzo[a]pyrene (BAPYR), benzo[e]pyrene (BEPYREN), perylene, benzo[ghi]perylene (BGHIPER), dibenzo[a,h]anthracene (AN-THAN) and coronene (CORONEN). This detailed mechanism has 397 species (named as KAUST hereafter). Considering its high computational cost, we used its reduced mechanism developed by Selvaraj et al. [39] (named RKAUST here after) [39], yet without losing generality, to study the high ring PAH precursors' effects for the soot formation and evolution in pressurized flames. RKAUST has 99 species and 625 reactions with PAH ranging from A1 to A7. Compared with the detailed KAUST mechanism, P2, A3, A3R5, FLTN, chrysene, perylene are reduced in RKAUST. As a result, the PAH precursors in RKAUST include naphthalene (A2), acephenanthrene (A2R5), pyrene (A4),A4R5, benzo[a]pyrene (BAPYR), benzo[e]pyrene (BEPYREN), benzo[ghi]perylene (BGHIPER), dibenzo[a,h]anthracene (ANTHAN) and coronene (CORONEN). In this study, RKAUST is used to reveal the effects of high ring PAH precursors on soot formation, in comparison to the NBP and RNBP mechanisms.

2.4. Soot-based Global Pathway Analysis (SGPA)

Global Pathway Selection (GPS) algorithm was firstly proposed by Gao, Yang, and Sun [23] as a mechanism reduction tool and then extended to Global Pathway Analysis (GPA) [24,25] to find the elementary reactions controlling the phenomena of interest in a complex reacting system and underlying connections among different species. In GPA, the most dominant global pathway (GP) in the reacting system is firstly selected with the GPS algorithm (more details in the next paragraph). Then, the radical production and consumption, heat release and elementary reactions associated with the most dominant GP can be calculated at all spatial positions to study the chemical kinetic effects. For completeness, the basics of the GPA algorithm is reviewed here first, before introducing the newly developed SGPA in this study.

As the first step, an element flux graph is constructed, where each node in the graph represents one species while the strengths of the edges connecting two nodes indicate the element (e.g., C, H and O in hydrocarbon combustion process) flux from one to another. The flux is calculated by

$$A_{e,i\to j} = \sum_{r} a_{e,r,i\to j},\tag{2}$$

where $a_{e,r,i\to j}$ is the contribution of the rth reaction to the element flux for element e from the ith species to the jth species, which is computed by

$$a_{e,r,i\to j} = \max(0, C_{e,r,i\to j}\dot{R}_r),\tag{3}$$

where \dot{R}_r is the net reaction rate of the rth reaction. Zero value is used if \dot{R}_r is negative to ensure one direction flux with certain starting species (i.e., the ith species) and ending species (i.e., the jth species). $C_{e,r,i\rightarrow j}$ is the element flux from the ith species to the jth species contributed by the r-th reaction, which is given by

$$C_{e,r,i\to j} = \begin{cases} n_{e,r,j} \frac{n_{e,r,i}}{n_{e,r}} & \nu_{r,j} \nu_{r,i} < 0; \\ 0 & \text{otherwise,} \end{cases}$$
 (4)

where $n_{e,r,i}$ is the number of the e-th element transferred out from the ith species in the rth reaction, $n_{e,r,j}$ is the number of the eth element transferred into the jth species in the rth reaction, $n_{e,r}$ is the number of the eth element transferred in the rth reaction, $v_{r,i}$ is the stoichiometric coefficient of the ith species in the rth reaction. The stoichiometric coefficient is positive for products and negative for reactants. In this way, $C_{e,r,i\rightarrow j}$ is zero when $v_{r,j}v_{r,i}$ is

positive, because the *i*th and *j*th species are in the same side in the reaction, indicating no element flux between them.

To extend this element flux graph construction to include soot, it is vital to build the relations from the gas-phase species element flux to/from soot. Following the way in Ref. [40], the soot unit is defined as a carbon cluster consisting of two carbon atoms. Note that this is only a unit for convenience to represent soot aggregates and it does not affect the following modeling and computation. We propose different ways to account for the carbon flux from PAH precursors and acetylene to soot (via condensation, nucleation and surface growth) and from soot to CO (via oxidation). In this way, the equations aforementioned need to be rearranged to include element flux due to the incorporation of soot in the edge flux graph. In Eq. (3), the net reaction rate of soot relevant reactions are considered by three types. Firstly, the carbon flux from PAH precursors to soot is introduced by the nucleation and condensation processes. In HMOM [33], the nucleation source term for the moments is

$$\dot{M}_{x,y}^{\text{nucl}} = \frac{1}{2} \beta_N [\text{DIMER}]^2 V_0^x S_0^y, \tag{5}$$

where V_0 and S_0 are the volume and surface of the smallest soot particles, respectively, [DIMER] is the molar concentration of PAH dimers, and β_N is the collision rate of the dimers, which is calculated by

$$\beta_{N} = 2.2 \sqrt{\frac{16\pi \, kT}{m_{D}}} d_{D}^{2},\tag{6}$$

where m_D and d_D are the dimer mass and diameter, respectively. k is the Boltzmann constant and T is the temperature. The smallest soot volume is given by

$$V_0 = 2W_C C_{\text{dimer}} / \rho_{\text{soot}}, \tag{7}$$

where W_C is the molecular weight of carbon, C_{dimer} is the average carbon atoms per dimer, and ρ_{soot} is the density of soot (1800 kg/m³). The smallest soot surface is thus given by

$$S_0 = (36\pi)^{1/3} / V_0^{2/3}. {8}$$

With Eq. (5), the soot molar concentration changing rate due to nucleation can be given by

$$\dot{R}_{\text{nucl}} = \dot{M}_{1,0}^{\text{nucl}} \rho_{\text{soot}} / 2W_{C}. \tag{9}$$

A factor of 2 with $W_{\rm C}$ is used here because the unit of soot is defined as two carbon atoms. In this study, condensation is defined as the collision of a soot particle with a PAH dimer. The moment source term due to condensation is calculated by

$$\dot{M}_{x,y}^{\text{cond}} = \sum_{s=0}^{\infty} \beta_{C_s} [(V_s + \delta V)^x (S_s + \delta S)^y - V_s^x S_s^y] [\text{DIMER}] N_s, \tag{10}$$

where β_{C_s} is the condensation rate of dimers with V_s as the soot particle size, which is given by

$$\beta_{C_s} = \sqrt{\frac{\pi kT}{2\mu_{D_s}}} (d_D + d_{c_s})^2, \tag{11}$$

where μ_{D_s} is the ratio of a dimer mass to a soot particle mass $\rho_{\rm soot} V_{\rm s.}$ $d_{\rm c_s}$ is the diameter of a soot particle. δV and δS are the volume and surface area changes of the particle contributed by condensation. Hence, the soot molar concentration changing rate contributed by condensation is expressed by

$$\dot{R}_{\text{cond}} = \dot{M}_{1.0}^{\text{cond}} \rho_{\text{soot}} / 2W_{\text{C}}. \tag{12}$$

Corresponding to Eq. (3), the carbon flux from PAH precursors to soot is given by

$$a_{C,\text{nucl+cond},i\to\text{soot}} = \alpha_p \max\left(0, C_{C,\text{nucl+cond},\text{PAH}_p\to\text{soot}} \frac{\dot{R}_{\text{nucl}} + \dot{R}_{\text{cond}}}{n_p^C}\right),$$
(13)

where $a_{C,\mathrm{nucl+cond},\mathrm{PAH}_p \to \mathrm{soot}}$ here is similar to $a_{e,r,i \to j}$ in Eq. (3), implying the carbon flux from the p-th PAH precursor to soot contributed by nucleation and condensation. α_p is the weight coefficient accounting for the contribution from p-th PAH precursor to the nucleation and condensation, which will be shown in Eq. 15. n_p^C is the carbon atom number in PAH $_p$. It is worthy mentioning that only carbon flux is considered here from PAH to soot due to the composition of soot. Typically, PAH precursors are ranging from naphthalene to cyclopenta[cd]pyrene, depending on the chemical reaction mechanisms used. To directly calculate carbon flux from PAH to soot, the assumption of steady-state dimerization is imposed: the dimer formation from PAH are balanced by dimer consumption from nucleation and condensation. In this way, the dimer formation rate $\dot{\omega}_{\mathrm{DIMER}}$ is given by

$$\dot{\omega}_{\text{DIMER}} = \beta_N [\text{DIMER}]^2 + \sum_{s=0}^{\infty} \beta_{C_s} N_s [\text{DIMER}]. \tag{14}$$

Also taking advantage of this assumption, the weight coefficient α_p is calculated based on the corresponding dimerization rate of the p-th PAH:

$$\alpha_p = \frac{\dot{R}_p^{\text{dimer}}}{\sum_p \dot{R}_p^{\text{dimer}}},\tag{15}$$

where $\dot{R}_{p}^{\text{dimer}}$ is the dimerization rate due to PAH_p, which is given by [41]

$$\dot{R}_p^{\text{dimer}} = \gamma_p (4\pi kT/m_p)^{1/2} (6m_p/\pi \rho_{\text{soot}})^{2/3} [\text{PAH}_p]^2, \tag{16}$$

where γ_p is the sticking coefficient of PAH $_p$ and is also detailed in Ref. [41]. m_p is mass of PAH $_p$, and [PAH $_p$] is the molar concentration of PAH $_p$.

Secondly, the carbon flux from C_2H_2 to soot, which is characterized by the surface growth process, is also calculated by the surface growth contribution to soot concentration:

$$\dot{M}_{x,y}^{sg} = \sum_{s=0}^{\infty} k_{sg} \chi S_s [(V_s + \delta V)^x (S_s + \delta S)^y - V_s^x S_s^y] [DIMER] N_s,$$
 (17)

where k_{sg} is the surface growth reaction rate, which is calculated based on the surface reactions with the gas-phase species via the H-Abastraction C_2H_2 -Addition (HACA) mechanism [42]. To better reproduce the experimental soot volume fraction at different pressures, it is reported in Refs. [14,43] that the empirical parameter α (representing the ratio of the actual active soot surface radical sites to the theoretical maximum soot surface radical sites) should be tuned. In this study, due to the uncertainty of rate constants for the reaction of the addition of C₂H₂ to soot radical sites (i.e., Soot-* + $C_2H_2 \rightarrow$ Soot-H, where Soot* is radical sites while Soot-H refers to hydrogenated sites on soot surface), the Arrhenius preexponential coefficient for this reaction is tuned to be 3.15×10^8 (units in cm, mol, s, K and kJ) following Ref. [41]. χ is the number of active sites per unit area on soot particles (1.7 \times 10⁻¹⁹ m⁻²). Similarly, the soot molar concentration changing rate due to surface growth is $\dot{R}_{sg} = \dot{M}_{1.0}^{sg} \rho_{soot}/2W_C$. The carbon flux from C_2H_2 to soot is thus given by

$$a_{C,sg,C_2H_2 \to soot} = max \left(0, C_{C,sg,C_2H_2 \to soot} \frac{\dot{R}_{sg}}{2} \right),$$
 (18)

where the rate of surface growth is divided by a factor 2 because there are two carbon atoms in C_2H_2 . For soot oxidation where the

carbon flux from soot to CO, the oxidation rate of soot is calculated based on the surface reactions with O_2 and OH, namely, Soot* + $O_2 \rightarrow Soot^*$ + 2CO and Soot-H + OH $\rightarrow Soot$ -H + CO. Different from the typical treatment for soot oxidation, the contributions from OH and O_2 are split because of the different carbon flux numbers in these two reactions. The moment source term due to soot oxidation by O_2 is given by

$$\dot{M}_{x,y}^{O_2} = -k_{O_2} \chi \frac{\delta V}{V_0} V_0^x S_0^{y+1} N_0 - \sum_{s=1}^{\infty} k_{O_2} \chi \left(x \frac{\delta V}{V_s} + y \frac{\delta S}{S_s} \right) V_s^x S_s^{y+1} N_s, \tag{19}$$

where k_{O_2} is a kinetic parameter calculated based on the soot surface reaction with O₂. Similarly, the contribution by OH oxidation is calculated by the same way as Eq. (19), but the kinetic parameter now is k_{OH} . The soot molar concentration changing rate contributed by O₂ and OH is then estimated by $\dot{R}_{OH} = \dot{M}_{1,0}^{\rm ox} \rho_{\rm soot}/2W_C$ and $\dot{R}_{O_2} = \dot{M}_{1,0}^{\rm ox} \rho_{\rm soot}/2W_C$, respectively. Hence, we have

$$a_{C,ox,soot \to CO} = \max(0, C_{C,O_2,soot \to CO} 2\dot{R}_{O_2} + C_{C,sg,soot \to CO} \dot{R}_{OH}). \tag{20}$$

After the construction of the element flux graph, hub species is then identified to form pathways from fuel to hub species and from hub species to soot. In this study, the PAH precursor or C_2H_2 with the largest value of normalized total element flux to soot is enforced as the hub species. In this way, every selected GP in the system has to pass through a PAH precursor or C_2H_2 and stop at the sink "species" soot, enabling us to see how carbon flows from fuel through PAH precursors or C_2H_2 to soot. The identification of GP after selecting the hub species is the same as the way introduced by Gao et al. [23], which is searching for the fastest (i.e., shortest time needed to transfer an unit atom from one node to another through a flux, based on the flux rate) path from the prescribed source species to the hub species and from the hub species to the sink species. The dominance of the GPs is then calculated by

$$D_{GP,e} = D_{\text{source},e} D_{GP/\text{source},e}, \tag{21}$$

where $D_{GP,e}$ is the ratio of the e-th element number in the source species to the total number of the e-th atom in all the initial species in the system. $D_{GP/\text{source},e}$ is the fraction of the e-th atoms that are going from the source species to sink species through this specific GP, which is given by

$$D_{GP/\text{source},e} = \left(\prod_{i,j \in GP} \frac{A_{e,i \to j}}{\sum_{k} A_{e,i \to k}}\right)^{(1/n_{GP})},\tag{22}$$

where $A_{e,i\rightarrow j}$ is defined in Eq. (2), n_{GP} is the number of conversion steps in this GP. The soot relevant flux is shown in Eqs. (13), (18) and (20).

Having identified the most dominant GPs, we can get a simplified representation of the reacting system, yet reflecting the key information of species conversions. With the SGPA method, we can identify the GPs that controls the carbon flux from fuel to soot, and subsequently extract the significant conversion steps and the involved elementary reactions for soot formation and evolution (see the schematic of SGPA in Fig. 1).

3. Pressurized co-flow diffusion sooting flames

3.1. Configuration

In this study, the ISF-4 Target Flame 2 [6–8] cases in the pressure range of 1–16 atm are simulated. This set of co-flow flames are fueled with ethylene diluted in nitrogen, which is surrounded by air co-flow. The fuel/air stream feeds through a central nozzle with an inner diameter of 4 mm and an outer diameter of 6 mm.

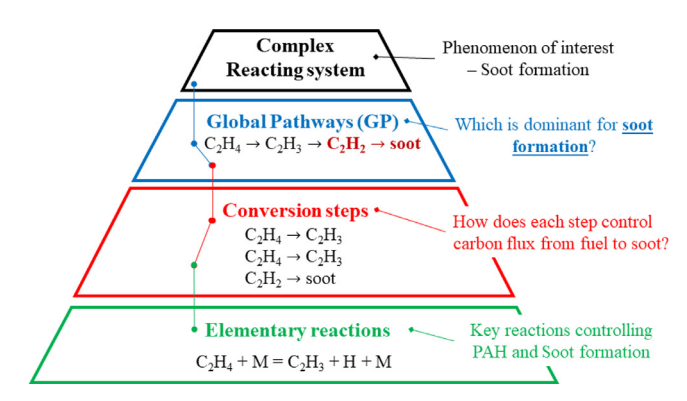


Fig. 1. Soot-based Global Pathway Analysis (SGPA): a hierarchical method to analyze complex chemical kinetics for sooting flames.

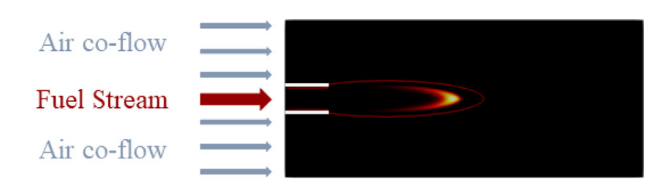


Fig. 2. Schematic of the configuration for the pressurized co-flow diffusion flames.

The total mass flow rate of the premixed ethylene (17.6% by mass) and nitrogen (82.4% by mass) stream is 7.78 mg/s. The Reynolds number for all the flames is 153 to keep them laminar. The configuration schematic is shown in Fig. 2. The inlet temperature is 300 K. More details on the flame configurations and operating conditions could be found in Refs. [6–8].

Two-dimensional (2D) direct numerical simulations of these flames with detailed finite-rate chemistry and molecular transport are carried out. A structured mesh is used with the domain size 59 mm axially and 15 mm radially, featuring 450 grid points along the axial direction and 80 grid points along the radial direction. In the region from fuel exit to the outlet boundary axially and from the central axis up to 10 mm radially (where the flame is supposed to locate), the mesh is homogeneous with a mesh size of 100 m. This mesh size is able to resolve the flame structures [12]. In other regions, the grid size is stretched radially with a rate of 1.3% for smooth transition. Boundary conditions of velocity, temperature and species mass fractions for the inlet are considered with uniform profiles. Isothermal with $T_{\text{wall}} = 400 \text{ K}$ is set for the nozzle walls (to take the heat loss into account), while adiabatic boundary conditions are used for the other walls (which are far away from the flame). No-slip boundary conditions are used for all the walls but not the top boundary, which is imposed with a free convective outflow condition.

3.2. Effect of pressure on soot and PAH formation

In this section, the pressure effect on soot formation and evolution in the pressurized flame are analyzed and discussed with the NBP mechanism. The experimental soot volume fraction is shown in Fig. 3, and qualitatively good agreement between the predicted and measured soot field is achieved, but also note that the agreement is better for lower pressures than higher pressures. More importantly, Within the pressure range from 1 to 8 atm, the peak soot volume fraction is located at the flame centerline, as measured in the experiment. However, the experimental maximum soot volume fraction is located the flame wings at 12 atm and 16 atm. This phenomenon is also well captured by the current simulations.

To further validate the numerical model, a quantitative comparison is given in Fig. 4, which shows the maximum soot volume

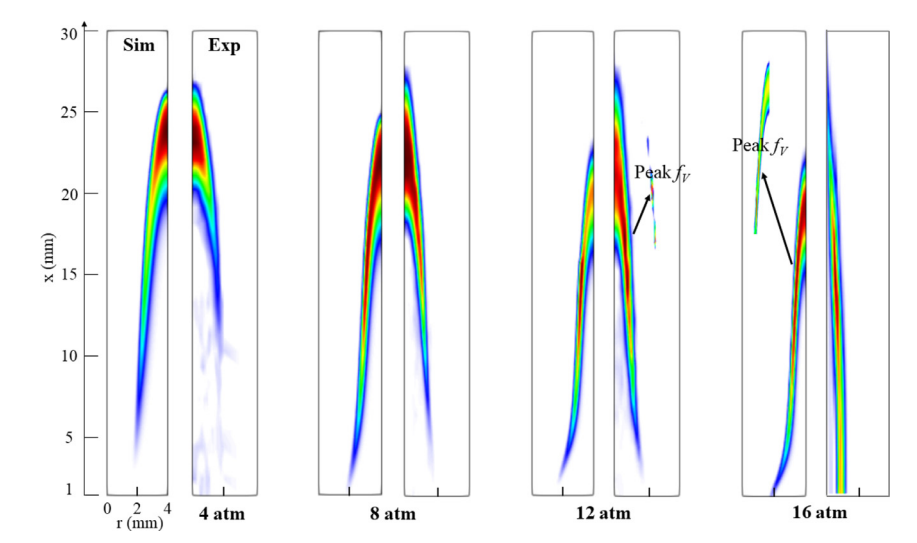


Fig. 3. Comparison of spatial soot distribution in simulations and experiments at 4, 8, 12 and 16 atm. Experimental data is from Refs. [6–8]. For a better qualitative comparison, different color scales are used for different pressures so that the peak soot volume fraction value corresponds to dark red color. To show the peak soot volume fraction positions, enlarged figures at 12 and 16 atm are re-scaled with different color levels.. (For interpretation of the references to color in this figure legend, the reader is referred to the web version of this article.)

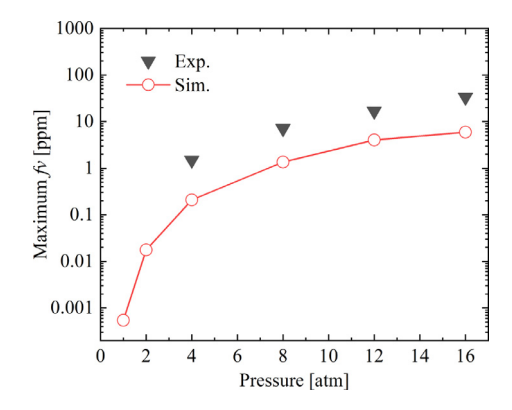


Fig. 4. Simulation (Sim.) and experiment (Exp.) maximum soot volume fraction f_V as a function of pressure. The maximum volume fraction values in simulations are 5.45×10^{-4} , 0.0176, 0.208, 1.357, 4.037, 5.93 ppm at 1, 2, 4, 8, 12 and 16 atm, respectively. Experimental data is from Refs. [6–8].

fraction f_V at different pressures. As seen, the scaling law of the maximum f_V as a function of the pressure, reported in many studies [2–5], is well captured by the current predictions.

On the other hand, the simulations still under-estimate the maximum soot yield. As discussed in Ref. [12], this could be due to the uncertainty involved in the complex physical processes from the gas-phase species chemical mechanisms to soot particle modeling. In order to separate these uncertainties and obtain in-depth understanding on the uncertainty of chemical kinetics, the predicted mole fractions of acetylene (C_2H_2) and several PAH species including A1, A2, and A3 are compared with the measured data, as shown in Fig. 5.

As seen in Fig. 5, the trend and order of magnitude of PAH species are again well reproduced by the simulations. However, the discrepancies at higher pressures are rather obvious, which indicates larger uncertainty of the gas-phase chemical kinetics at higher pressures. Specifically, the simulations over-predict A1 and C₂H₂, but under-predict the PAH species with multiple aromatic rings (e.g., A2 and A3), especially at higher pressures. Similar phenomena were observed in Ref. [12] with the same chemical mechanism, which suggests that although the NBP mechanism [22] is widely validated, the conversion rates from C₂H₂ and A1 to higher PAH rings species are somehow underestimated at elevated pressures.

 Table 1

 List of species and their chemical formulas in the GPs in this study.

Species name	Formula
benzene	A1
phenyl radical	A1-
ethynylbenzene	$A1C_2H$
phenylvinyl	$A1C_2H_2$
2-ethynylphenyl	A1C ₂ HY
Indene	C_9H_8
Indenyl	C_9H_7
napthalene	A2
napthyl	A2-
2-napthylvinyl	A2C2H2A
acenaphthylene	A2R5
phenanthrene	A3
pyrene	A4
anthanthracene	ANTHAN
pyrenyl radical	A4-
ethynyl-pyrene radicals	PYC2H-4
benzo[e]pyrenyl radical	BEPYRENJ
benzo[ghi]perylenyl radicals	BGHIPEJS

To scrutinize the pressure effect on the chemical kinetics, a single-point SGPA is conducted at the maximum A2 location in the domain, because the large discrepancy of the predicted A2 at high pressures is observed at this position. A spatially SGPA for the whole domain to identity dominant global pathways (GPs) at different locations in the sooting flames will be conducted later in this section. The single-point SGPA is intended to show how A2 is formed from fuel, thus identify the key GPs that dominates the formation of A2. In this sense, we can further understand the uncertainty of specific conversion steps and elementary reactions. The single-point SGPA method shows that with the increased pressure, the dominant GP from fuel to A2 shift from $C_2H_4 \rightarrow C_2H_3 \rightarrow C_2H_2$ \rightarrow PC_3H_4 \rightarrow C_3H_3 \rightarrow A1 \rightarrow A1 - \rightarrow C_9H_8 \rightarrow C_9H_7 \rightarrow A2 at 1 atm, to $C_2H_4 \rightarrow C_2H_3 \rightarrow C_2H_2 \rightarrow A1C_2H_2 \rightarrow A1C_2H \rightarrow A1C_2HY \rightarrow A2 \rightarrow$ A2 at 4 atm and to $C_2H_4 \rightarrow C_2H_3 \rightarrow C_2H_2 \rightarrow C_9H_8 \rightarrow C_9H_7 \rightarrow$ A2 at 8 atm and 12 atm (a list of the species in the GPs in this study is given in Table 1).

At 1 atm, the first ring A1 formation is dominated by C_3H_3 recombination reactions, which finally goes through A1 + C_3H_3 = C_9H_8 , hydrogen abstraction of C_9H_8 to form C_9H_7 , and then forms A2. The reactions involved in these conversion steps at 1

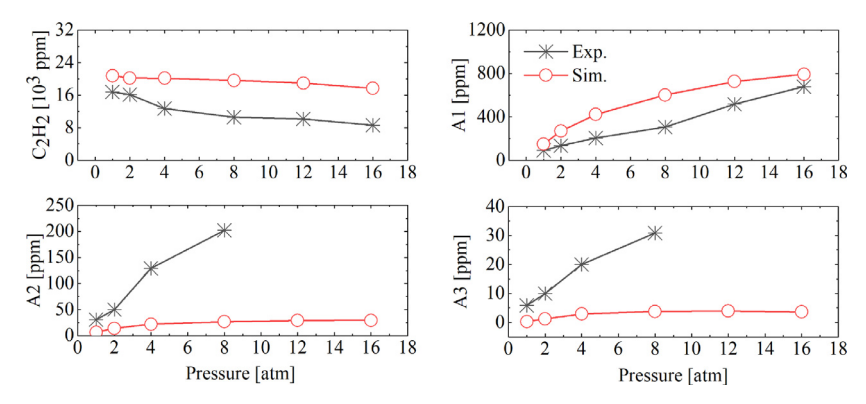


Fig. 5. Simulation (Sim.) and experiment (Exp.) maximum mole fractions of C_2H_2 , A1, A2 and A3, at different pressures. The experimental data is from Refs. [6–8]. A2 and A3 measurements are not available at 12 and 16 atm.

atm should be with less uncertainty, due to its good predictability for A2 in comparison to the experimental data. It is interesting to note that A2 is also formed through C9H7 and C9H8 reactions at 8 atm and 12 atm, but large discrepancy for A2 prediction is observed at 8 atm (although lack of experimental data, the large discrepancy at 12 atm can be expected as presented by the trend in Fig. 5). Since C₂H₂ is also accurately captured by the prediction at 8 and 12 atm (as shown in Fig. 5), we can then draw a reliable conclusion that the largest uncertainty is from the conversion step $C_2H_2 \rightarrow C_9H_8$. A closer look at the relevant elementary reactions indicates that the reaction $C_2H_2 + A1CH_2 = C_9H_8 + H$ is the only reaction involved in this conversion step. Based on the NBP mechanism development process [22], the rate of this reaction is estimated by analogy based on the reactions of cyclopentadienyl (c-C₅H₅) [44]. As a result, this reaction, as identified in this study, merits further investigation experimentally or through statistical theory calculations to reduce its rate coefficient uncertainty. The 4 atm case also shows obvious discrepancy, which could be due to the conversion steps between C₂H₂ to A2. However, the identification of specific reactions with large uncertainty is hindered by the lack of experimental data for the involved intermediate species.

We then employed SGPA to analyze the soot formation and evolution dominant GPs at all the spatial locations in the flames. As shown in Fig. 6, different GPs dominate the conversion from fuel to soot at different locations. With SGPA, we can clearly observe how fuel pass carbon element to soot through different species and conversion steps. The nucleation and condensation regions coincide with GP3, GP4 and GP5 positions (see Fig. 6(b)(c)), where the final conversions steps involves A2 and A2R5, while the surface growth regions spatial positions agree well (see Fig. 6(d)) with the GP6 positions with C_2H_2 in the final conversion steps. To better illustrate the GPs in the following, the conversion steps: $C_2H_4 \rightarrow C_2H_3 \rightarrow C_2H_2$ are lumped as "CV1".

At 1 atm, as shown in Fig. 6(b), the nucleation are mainly controlled by GP3 (CV1 \rightarrow PC₃H₄ \rightarrow C₃H₃ \rightarrow A1 \rightarrow A1- \rightarrow C₉H₈ \rightarrow C₉H₇ \rightarrow A2R5 \rightarrow soot) and GP4 (CV1 \rightarrow A1C₂H₂ \rightarrow A1C₂H \rightarrow A1C₂HY \rightarrow A2- \rightarrow A2C₂H₂A \rightarrow A2R5 \rightarrow soot). Specifically, the maximum nucleation near the flame centerline is mainly controlled by GP3 and GP4, in which the major PAH precursors is A2R5. Although the same PAH precursor shared (i.e., A2R5), GP3 forms A2R5 by the reactions through A1- + C₃H₃ = C₉H₈, hydrogen abstraction of C₉H₈ and C₉H₇ + C₃H₃ = A2R5 + 2H, while GP4 involves the HACA mechanism for PAH growth to form A2R5. It is also noted that the formation of the first ring A1 from the C₃H₃ recombination (i.e., C₃H₃ + C₃H₃ = A1 in GP2 and GP3) plays a significant role, which is also observed in the study of Liu et al. [13]. As shown in Fig. 6(c), condensation is mainly dominated by GP4 and GP5 (CV1 \rightarrow C₃H₃ \rightarrow A1 \rightarrow A1- \rightarrow C₉H₈ \rightarrow C₉H₇ \rightarrow A2 \rightarrow

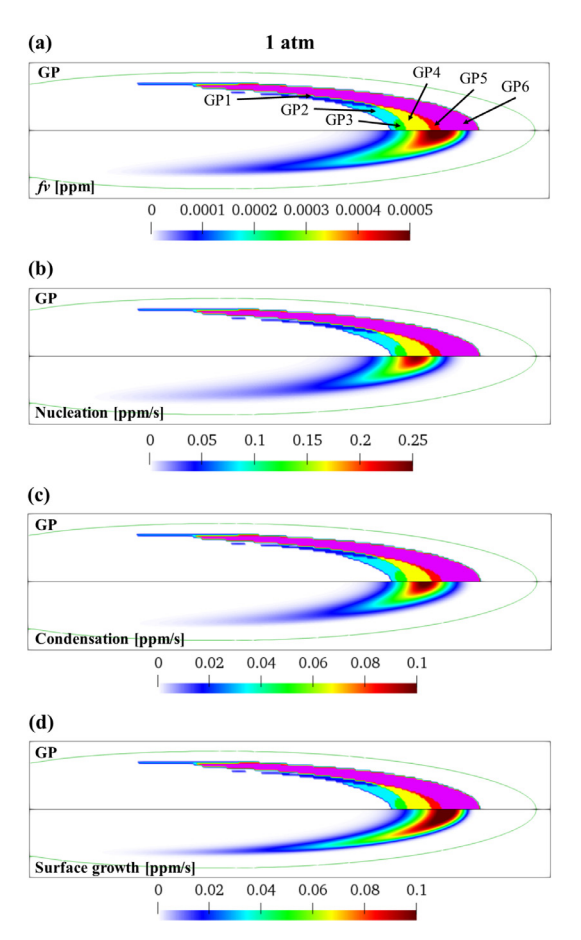


Fig. 6. The spatial distribution of dominant GPs from fuel (i.e., C_2H_4) to soot at 1 atm. (a) Soot volume fraction, (b) nucleation source term, (c) condensation source term and (d) surface growth source term are also shown for comparison. $C_2H_4 \rightarrow C_2H_3 \rightarrow C_2H_2$ is lumped as CV1. **GP1:** CV1 \rightarrow A1C₂H₂ \rightarrow A1C₂H \rightarrow A1C₂H \rightarrow A2- \rightarrow A2 \rightarrow soot; **GP2:** CV1 \rightarrow C₃H₃ \rightarrow A1 \rightarrow A1 \rightarrow A1 \rightarrow C₉H₈ \rightarrow C₉H₇ \rightarrow A2 \rightarrow soot; **GP3:** CV1 \rightarrow PC₃H₄ \rightarrow C₃H₃ \rightarrow A1 \rightarrow A1 \rightarrow A1 \rightarrow C₉H₈ \rightarrow C₉H₇ \rightarrow A2R5 \rightarrow soot; **GP4:** CV1 \rightarrow A1C₂H₂ \rightarrow A1C₂H \rightarrow A1C₂H \rightarrow A1C₂H \rightarrow A2R5 \rightarrow soot; **GP5:** CV1 \rightarrow C₃H₃ \rightarrow A1 \rightarrow A1 \rightarrow A1 \rightarrow C₉H₈ \rightarrow C₉H₇ \rightarrow A2 \rightarrow A2 \rightarrow A2C₂H₂A \rightarrow A2R5 \rightarrow soot; **GP6:** CV1 \rightarrow soot. The olive green solid line indicates the stoichiometric mixture fraction location. (For interpretation of the references to colour in this figure legend, the reader is referred to the web version of this article.)

 $A2- \rightarrow A2C_2H_2A \rightarrow A2R5 \rightarrow soot)$. In GP5, C_3H_3 recombination and reactions through C_9H_8 and C_9H_7 are also significant, which is similar to GP2 and GP3. As seen in Fig. 6(d), surface growth is only dominated by the fuel H abstraction to form C_2H_2 , which then reacts with the soot surface active sites (i.e., GP6 (CV1 \rightarrow soot)).

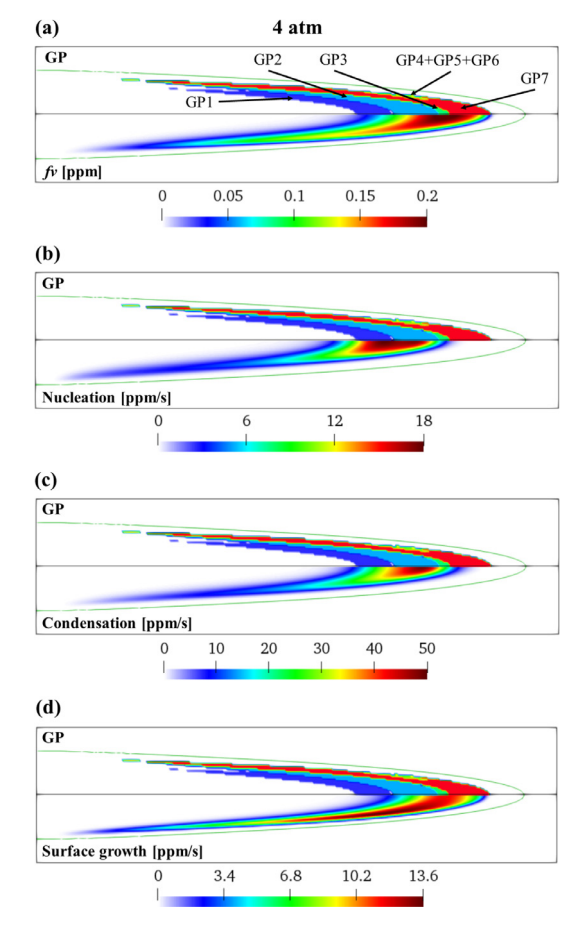


Fig. 7. The spatial distribution of dominant GPs from fuel (i.e., C_2H_4) to soot at 4 atm. (a) Soot volume fraction, (b) nucleation source term, (c) condensation source term and (d) surface growth source term are also shown for comparison. $C_2H_4 \rightarrow C_2H_3 \rightarrow C_2H_2$ is lumped as CV1. **GP1**: CV1 \rightarrow $C_9H_8 \rightarrow C_9H_7 \rightarrow A2 \rightarrow$ soot; **GP2**: CV1 \rightarrow A1 $C_2H_2 \rightarrow$ A1 $C_2H \rightarrow$ A1 $C_2H \rightarrow$ A1 $C_2H \rightarrow$ A2 $C_2H_2 \rightarrow$ A2 $C_2H_2 \rightarrow$ A2F5 \rightarrow soot; **GP3**: CV1 \rightarrow A1 $C_2H_2 \rightarrow$ A1 $C_2H \rightarrow$ CH3 \rightarrow CG4 \rightarrow CH4 \rightarrow CH3 \rightarrow CG4 \rightarrow CG4 \rightarrow CG4 \rightarrow CH4 \rightarrow CH3 \rightarrow CG4 \rightarrow CG4 \rightarrow CG7 \rightarrow CG7

The spatial distribution of SGPA-identified most dominant GPs at 4 atm is shown in Fig. 7. As seen in Fig. 7(b), the nucleation process is controlled by GP1 (CV1 \rightarrow C₉H₈ \rightarrow C₉H₇ \rightarrow A2 \rightarrow soot) and GP2 (CV1 \rightarrow A1C₂H \rightarrow A1C₂HY \rightarrow A2- \rightarrow A2C₂H₂A \rightarrow A2R5 → soot). Similar to the 1 atm case, the HACA mechanism (i.e., GP2) still plays a significant role in the PAH growth. However, the major difference is that the first ring PAH (i.e., A1) formation is no more dependent on C₃H₃ recombination, because the carbon fluxes do not flow to C₃H₃ in GP1 and GP2. The pressure effect also alter the PAH growth through C₉H₈ and C₉H₇, where C₉H₈ is formed by A1CH₂ + $C_2H_2 = C_9H_8$ + H instead of the reaction through C₃H₃ and A1 at 1 atm. GP2 prevails in the condensation regions as shown in Fig. 7(c), where C₉H₇ and C₉H₈ play important roles again. As for surface growth, the major dominant pathway GP7 $(CV1 \rightarrow soot)$ is the same as the 1 atm case at the centerline. However, it is seen that the flame wing surface growth regions now is controlled by other GPs (GP4+GP5+GP6). The major difference of GP4+GP5+GP6 from GP7 is the pathway to form C2H2, caused by the pressure effect in the third body reaction $C_2H_3 + H + M = C_2H_4$ + M which suppressed the generation of C_2H_3 at high pressures $(C_2H_3$ goes to C_2H_2 by CV1). As a result, the reactions of fuel to other products such as H₂C₂ in GP4, CH₃ in GP5 and GP6 become

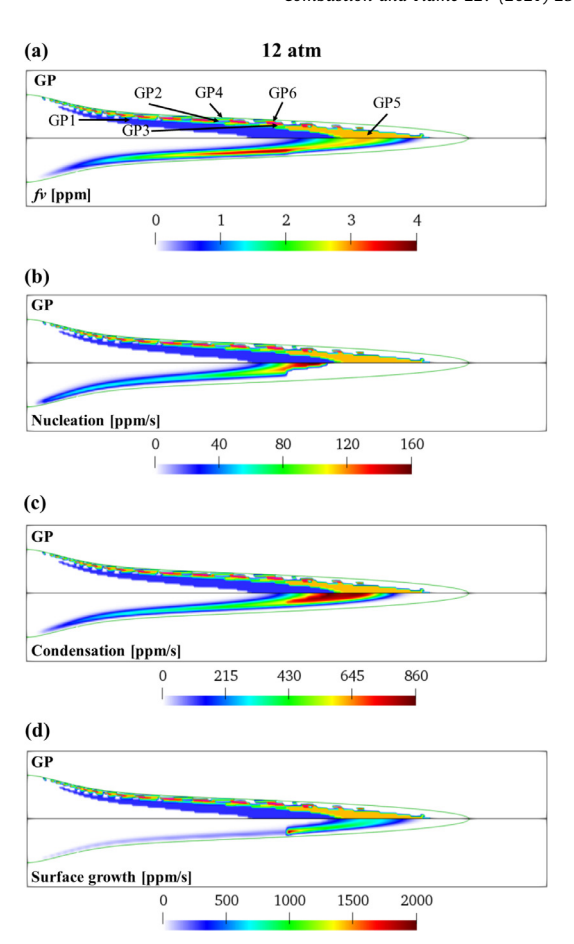


Fig. 8. The spatial distribution of dominant GPs from fuel (i.e., C_2H_4) to soot at 12 atm. (a) Soot volume fraction, (b) nucleation source term, (c) condensation source term and (d) surface growth source term are also shown for comparison. $C_2H_4 \rightarrow C_2H_3 \rightarrow C_2H_2$ is lumped as CV1. **GP1**: CV1 \rightarrow C₃H₈ \rightarrow C₃H₇ \rightarrow A2 \rightarrow soot; **GP2**: CV1 \rightarrow A1C₂H₂ \rightarrow A1C₂H \rightarrow A1C₂HY \rightarrow A2 \rightarrow soot; **GP3**: CV1 \rightarrow A1C₂H₂ \rightarrow A1C₂HY \rightarrow A1 \rightarrow A1 \rightarrow A1 \rightarrow A1 \rightarrow A2 \rightarrow soot; **GP5**: CV1 \rightarrow soot; **GP5**: CV1 \rightarrow SCH₂ \rightarrow C₃H₃ \rightarrow PC₃H₄ \rightarrow C₂H₂ \rightarrow soot. The olive green solid line indicates the stoichiometric mixture fraction line. (For interpretation of the references to colour in this figure legend, the reader is referred to the web version of this article.)

significant to form C_2H_2 ($H_2C_2 \rightarrow C_2H_2$ in GP4, $CH_3 \rightarrow SCH_2 \rightarrow C_3H_3 \rightarrow PC_3H_4 \rightarrow C_2H_2$ in GP5 and $CH_3 \rightarrow SCH_2 \rightarrow C_3H_3 \rightarrow C_3H_2 \rightarrow C_2H_2$ in GP6) for soot surface growth. In addition, although the surface growth peaks at the flame wing, the soot volume fraction still show its maximum values at the flame centerline. This is due to the fact that nucleation and condensation still dominate the soot formation and evolution at 4 atm, as shown in Fig. 7.

At 12 atm, the dominant GPs with nucleation, condensation and surface growth are still well represented by certain GPs (i.e., GP1 $(CV1 \rightarrow C_9H_8 \rightarrow C_9H_7 \rightarrow A2 \rightarrow soot), GP4 (CV1 \rightarrow A1C_2H_2 \rightarrow$ $A1C_2HY \rightarrow A2- \rightarrow A2 \rightarrow soot)$ and GP5 (CV1 $\rightarrow soot)$ in Fig. 8). Due to the narrow flame, the nucleation and condensation regions is also narrow, where GP1 in Fig. 8 dominates the nucleation and it is the exact same GP as the 4 atm case for nucleation. Although the rates of nucleation and condensation increase at 12 atm compared with 4 atm, the dominant chemical kinetics are similar, in which HACA, C_9H_8 and C_9H_7 are significant. The surface growth is also similar to the 4 atm case, in which GP6 ($C_2H_4 \rightarrow CH_3 \rightarrow$ $SCH_2 \rightarrow \ C_3H_3 \rightarrow \ PC_3H_4 \rightarrow \ C_2H_2 \rightarrow \ soot)$ prevails at the wing. The major difference found in the 12 atm case is the condensation start to compete with surface growth at the flame wing (GP4 (CV1 \rightarrow $A1C_2H_2 \rightarrow A1C_2HY \rightarrow A2- \rightarrow A2 \rightarrow soot)$ in Fig. 8). This was also found by Eaves et al. [15], which indicates that condensation could

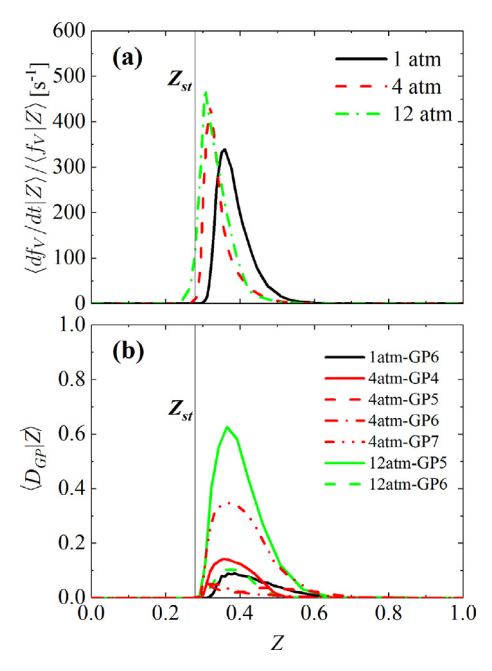


Fig. 9. (a) Conditional soot surface growth rates $\langle df_V/dt|Z\rangle$ normalized by conditional mean volume fraction $\langle f_V|Z\rangle$ at 1, 4 and 12 atm; (b) Conditional dominance of surface growth related global pathways $\langle D_{CP}|Z\rangle$ at 1, 4 and 12 atm. The vertical black line indicates the stoichiometric mixture fraction $Z_{\rm st}=0.28$.

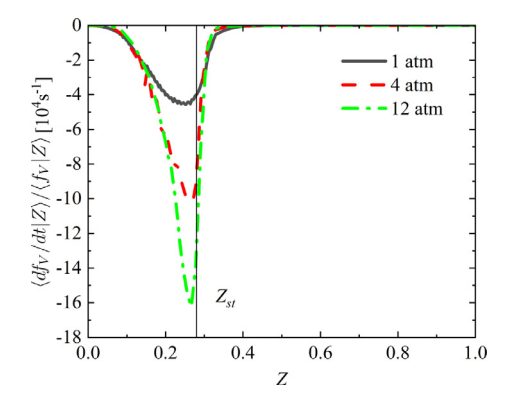


Fig. 10. Conditional soot oxidation rates $\langle df_V/dt|Z\rangle$ normalized by conditional mean volume fraction $\langle f_V|Z\rangle$ at 1, 4 and 12 atm. The vertical black line indicates the stoichiometric mixture fraction $Z_{\rm st}=0.28$.

extend to the flame wing at high pressures. As noted in soot source term values, surface growth at the wing is dominant over nucleation and condensation, leading to soot volume fraction peaks at flame wings instead of centerline as in the lower pressure cases.

Since soot is very sensitive to the gas-phase composition, it is critical to understand the roles that the most dominant GPs in the mixture fraction space. The most dominant GPs as identified in Figs. 6–8 at different pressures are plotted in the mixture fraction (Z) space, with the conditional mean dominance values of GPs. The conditional mean values of surface growth, condensation, nucleation and oxidation source terms in the Z space are also discussed here. The conditional mean values of surface growth and oxidation rates $\langle df_V/dt|Z\rangle$ in the Z space are normalized by the conditional mean volume fraction $\langle f_V | Z \rangle$, and are plotted in Fig. 9(a) and Fig. 10, respectively. It is seen that in Fig. 9(a), the normalized surface growth source term has only trivial change with increasing pressure, indicating that the surface growth increase is mainly due to the high soot volume at high pressures instead of the surface growth coefficient. However, the normalized oxidation source terms still scales with increasing pressure significantly, as shown in

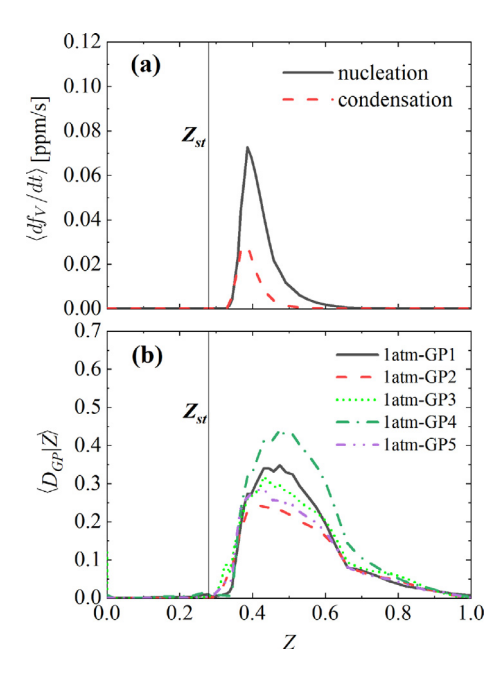


Fig. 11. (a) Conditional soot nucleation and condensation rates $\langle df_V/dt|Z\rangle$ at 1 atm; (b) Conditional dominance of nucleation and condensation related global pathways $\langle D_{CP}|Z\rangle$ at 1 atm. The vertical black line indicates the stoichiometric mixture fraction $Z_{\rm st}=0.28$.

Fig. 10. As seen, the saturated trend of maximum soot volume fraction with increasing pressure is due to the significantly increased oxidation rate over the slightly increased surface growth. The conditional dominance of GPs relevant to surface growth, defined in Eq. (21), are presented in Fig. 9(b). For the 1 atm case, H abstraction of C_2H_4 to C_2H_3 , with the following generation of C_2H_2 is the most dominant pathway to generate C_2H_2 , which promotes soot surface growth through the HACA mechanism. At 4 and 12 atm, the other C_2H_2 generation mechanism starts to play a role, due to the third body reactions (i.e., $C_2H_3 + H + M = C_2H_4 + M$) discussed above. However, it is seen here that these reactions are still not as significant as $C_2H_4 \rightarrow C_2H_3 \rightarrow C_2H_2$.

Soot nucleation and condensation are mainly controlled by the PAH dimer concentrations. Considering the increased gas density and thus increased PAH concentration, nucleation and condensation rates should increase at higher pressures. The 1 atm conditional nucleation and condensation $\langle df_V/dt|Z\rangle$ in the mixture fraction (Z) space is presented in Fig. 11(a), showing that at 1 atm, nucleation is dominant over condensation, in terms of both its magnitude and support width in Z space. The dominance of nucleation and condensation related GPs $\langle D_{GP}|Z\rangle$ are shown in Fig. 11(b). It is seen that 1atm-GP4 (i.e., GP4 in Fig. 6: CV1 \rightarrow A1C₂H₂ \rightarrow A1C₂H \rightarrow A1C₂HY \rightarrow A2- \rightarrow A2C₂H₂A \rightarrow A2R5 \rightarrow soot) where PAH growth is controlled by the HACA mechanism, is the most significant GP, although the other GPs have comparable dominance magnitude.

As for 4 atm, the condensation process now dominates over the nucleation both spatially in the Z space and numerically in magnitude, as shown in Fig. 12(a). The dominance of the identified GPs in the Z space showed that at 4 atm, the most dominant GP is 4atm-GP2 (i.e., GP2 in Fig. 7: CV1 \rightarrow A1C₂H₂ \rightarrow A1C₂H \rightarrow A1C₂HY \rightarrow A2- \rightarrow A2C₂H₂A \rightarrow A2R5 \rightarrow soot), which is exactly the same as the most dominant GP at 1 atm (i.e., 1atm-GP4). This indicates that with the increasing pressure from 1 to 4 atm, although the increased soot yield enhances the condensation process, the most dominant GPs to form the nucleation/condensation precursor (i.e., A2R5) are the same. At 12 atm (see Fig. 13), the dominance of the GPs did not show obvious difference. Note that the global path-

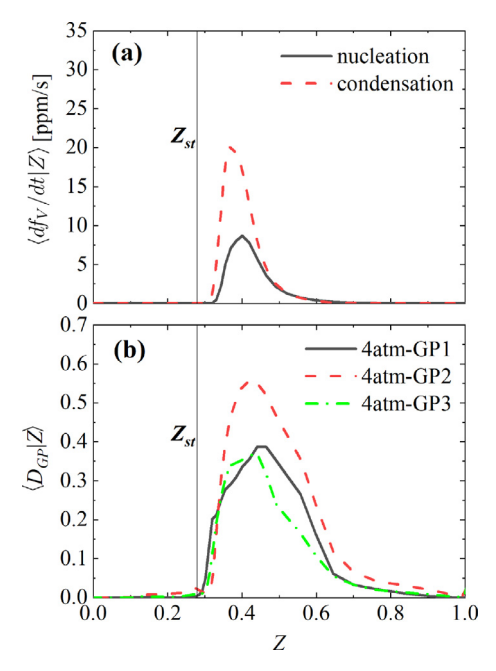


Fig. 12. (a) Conditional soot nucleation and condensation rates $\langle df_V/dt|Z\rangle$ at 4 atm; (b) Conditional dominances of nucleation and condensation related global pathways $\langle D_{GP}/dt|Z\rangle$ at 4 atm. The vertical black line indicates the stoichiometric mixture fraction $Z_{\rm st}=0.28$.

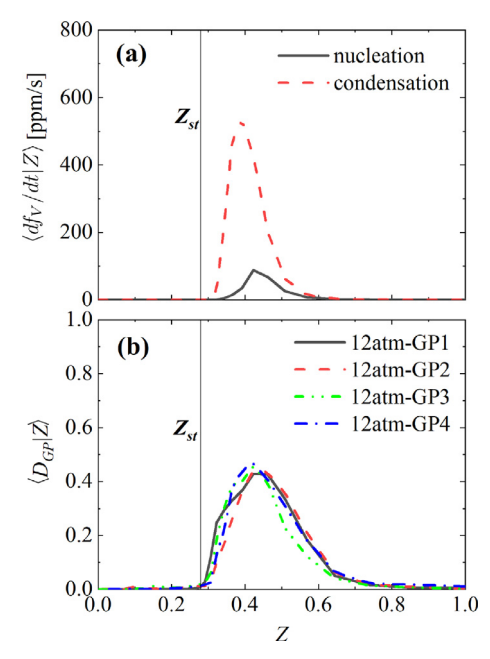


Fig. 13. (a) Conditional soot nucleation and condensation rates $\langle df_V/dt|Z\rangle$ at 12 atm; (b) Conditional dominances of nucleation and condensation related global pathways $\langle D_{GP}/dt|Z\rangle$ at 12 atm. The vertical black line indicates the stoichiometric mixture fraction $Z_{\rm st}=0.28$.

way 12atm-GP4, which dominates at the flame wing (see Fig. 8), showed equivalent dominance compared with other GPs, implying that at high pressures, condensation contribute significantly to the flame wing soot evolution.

3.3. Effect of mechanism reduction

In this section, we employ the reduced mechanism RNBP [37] and analyze the diffusion flame data with the SGPA method. In their reduction [37], the NBP mechanism was reduced firstly

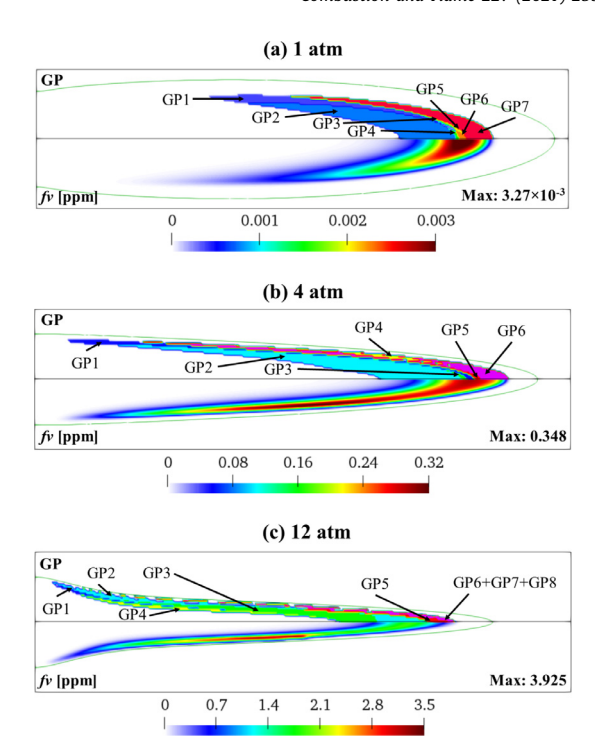


Fig. 14. The dominant GPs from fuel (i.e., C_2H_4) to soot at different spatial positions at (a) 1 atm, (b) 4 atm and (c) 12 atm, calculated with the RNBP mechanism. The GPs details are shown in Table 2. Soot volume fraction field with the maximum soot volume fraction are also shown in the figure. The olive green solid line indicates the stoichiometric mixture fraction location. (For interpretation of the references to color in this figure legend, the reader is referred to the web version of this article.)

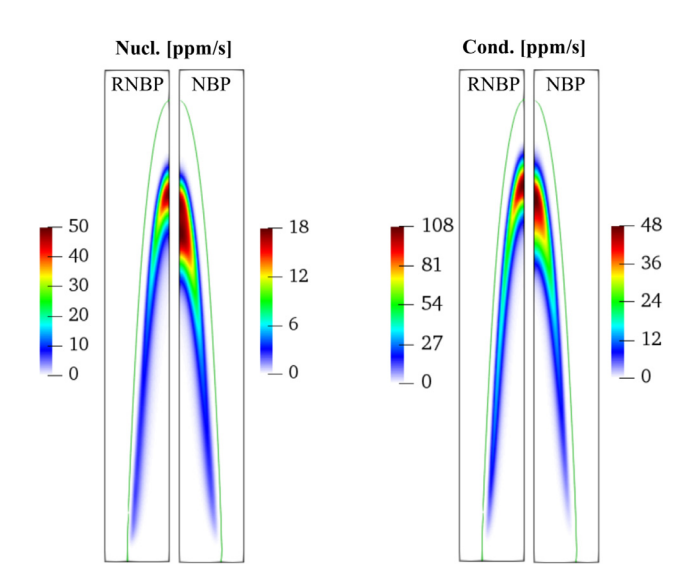
by deleting all the species with higher aromatic rings than A2 manually. Directed Relation Graph with Error Propagation (DRGEP) [45] and isomer lumping were then used to automatically reduce the mechanism. The automatic DRGEP mechanism reduction *ad hoc* chose C_2H_2 and A2 as the target species to retain its soot prediction capability. As seen, the major difference of this reduced mechanism from NBP is that it only contains A2 as the PAH precursor for dimerization. A2R5, C_9H_7 and C_9H_8 , which were identified as significant species in the previous section for the pressurized sooting flames with NBP, were all deleted in RNBP.

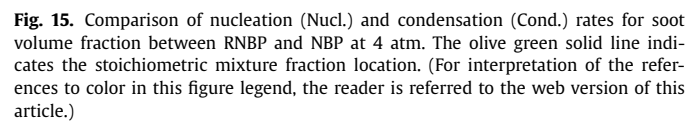
First of all, the spatial distribution of dominant GPs is shown in Fig. 14, together with the soot volume fraction f_V field. The GPs at different spatial locations showed the same chemical kinetics as the full NBP mechanism for the first ring (i.e., A1) formation reactions. In addition, the nucleation and condensation process also appears at the flame wing at 12 atm (see GP2 in Fig. 14(c)). Compared with the detailed NBP mechanism, the reduced mechanism predict slightly higher peak f_V than the detailed NBP mechanism. However, the spatial distribution of soot is very different from the results predicted by NBP, especially for the 4 atm case. NBP predicted the maximum f_V at the flame centerline (see Fig. 3 for comparison), while with RNBP, f_V peaks at the flame wing. As the results by RNBP are different from the experimental observation, the mechanism reduction process for RNBP must have incurred critical inaccuracy for soot prediction, especially at elevated pressures.

Because both NBP and RNBP predict the peak soot volume fraction correctly at 1 and 12 atm and RNBP tends to overpredict the flame wing soot at 4 atm, we focus at 4 atm here to analyze the underlying reasons leading to the prediction discrepancy by RNBP. A comparison of the soot source terms between NBP and RNBP at 4 atm are shown in Figs. 15 and 16 for nucleation (nucl.)/condensation(cond.) and surface growth (SG)/oxidation (ox.), respectively. As seen, nucleation and conden-

Table 2 GPs identified by SGPA for RNBP at different spatial locations at 1, 4 and 12 atm (see Fig. 14). $C_2H_4 \rightarrow C_2H_3 \rightarrow C_2H_2$ is lumped as CV1.

```
1 atm
                                      GP1: CV1 \rightarrow C<sub>3</sub>H<sub>3</sub> \rightarrow A1 \rightarrow A1- \rightarrow A1C<sub>2</sub>H<sub>2</sub> \rightarrow A1C<sub>2</sub>H \rightarrow A1C<sub>2</sub>HY \rightarrow A2- \rightarrow A2 \rightarrow soot
                                      \textbf{GP2} \text{: CV1} \, \rightarrow \, \text{A1C}_2\text{H}_2 \, \rightarrow \, \text{A1C}_2\text{H} \, \rightarrow \, \text{A1C}_2\text{HY} \, \rightarrow \, \text{A2-} \, \rightarrow \, \text{A2} \, \rightarrow \, \text{soot}
                                     \textbf{GP3} \colon \text{CV1} \to \text{C}_3\text{H}_3 \to \text{A1} \to \text{A1-} \to \text{A1C}_2\text{H}_2 \to \text{A1C}_2\text{H} \to \text{A1C}_2\text{HY} \to \text{A2} \to \text{soot}
                                      GP4: CV1 \rightarrow A1C_2H_2 \rightarrow A1C_2H \rightarrow A1C_2HY \rightarrow A2 \rightarrow soot
                                      \textbf{GP5} \colon \text{CV1} \, \to \, \text{C}_3\text{H}_3 \, \to \, \text{A1} \, \to \, \text{A1-} \, \to \, \text{A1CH}_2 \, \to \, \text{A2} \, \to \, \text{soot}
                                     GP6: CV1 \rightarrow PC<sub>3</sub>H<sub>4</sub> \rightarrow C<sub>3</sub>H<sub>3</sub> \rightarrow A1 \rightarrow A1- \rightarrow A1CH<sub>2</sub> \rightarrow A2 \rightarrow soot
                                     GP7: CV1 \rightarrow soot
4 atm
                                      GP1: CV1 \rightarrow A2- \rightarrow A2 \rightarrow soot
                                     \textbf{GP2} \text{: CV1} \rightarrow \text{A1C}_2\text{H}_2 \rightarrow \text{A1C}_2\text{H} \rightarrow \text{A1C}_2\text{HY} \rightarrow \text{A2-} \rightarrow \text{A2} \rightarrow \text{soot}
                                     \textbf{GP3:} \ \text{CV1} \rightarrow \text{PC}_3\text{H}_4 \rightarrow \text{C}_3\text{H}_3 \rightarrow \text{A1} \rightarrow \text{A1-} \rightarrow \text{A1C}_2\text{H}_2 \rightarrow \text{A1C}_2\text{H} \rightarrow \text{A1C}_2\text{HY} \rightarrow \text{A2-} \rightarrow \text{A2} \rightarrow \text{soot}
                                      \textbf{GP4} \hbox{:}\ C_2H_4 \rightarrow CH_3 \rightarrow SCH_2 \rightarrow C_3H_3 \rightarrow C_2H_2 \rightarrow soot
                                      \textbf{GP5} \colon \text{CV1} \to \text{PC}_3\text{H}_4 \to \text{C}_3\text{H}_3 \to \text{A1} \to \text{A1-} \to \text{A1CH}_2 \to \text{A2} \to \text{soot}
                                     GP6: CV1 \rightarrow soot
12 atm
                                     \textbf{GP1} \colon \text{CV1} \, \to \, \text{C}_5\text{H}_5 \, \to \, \text{A1CH}_2 \, \to \, \text{A2} \, \to \, \text{soot}
                                      GP2: CV1 \rightarrow A2- \rightarrow A2 \rightarrow soot
                                      GP3: CV1 \rightarrow A1C<sub>2</sub>H<sub>2</sub> \rightarrow A1C<sub>2</sub>H \rightarrow A1C<sub>2</sub>HY \rightarrow A2- \rightarrow A2 \rightarrow soot
                                     GP4: CV1 \rightarrow A1CH<sub>2</sub> \rightarrow A2 \rightarrow soot
                                      GP5: CV1 \rightarrow soot
                                     \textbf{GP6} \hbox{:}\ C_2H_4 \rightarrow CH_3 \rightarrow PC_3H_4 \rightarrow C_3H_3 \rightarrow C_2H_2 \ soot
                                     GP7: C_2H_4 \rightarrow CH_3 \rightarrow SCH_2 \rightarrow C_3H_3 \rightarrow C_2H_2 soot
                                     \textbf{GP8} \colon C_2H_4 \to CH_3 \to C_3H_3 \to C_2H_2 \to soot
```





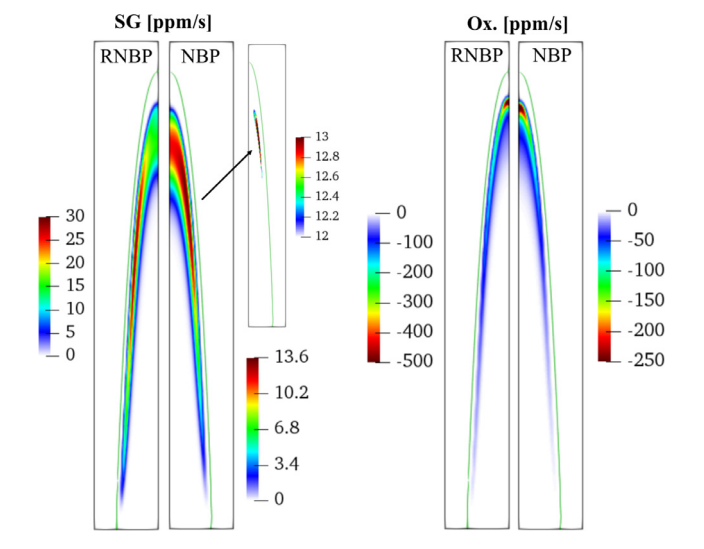


Fig. 16. Comparison of surface growth (SG) and oxidation (Ox.) rates for soot volume fraction between RNBP and NBP at 4 atm. The olive green solid line indicates the stoichiometric mixture fraction location. To show the peak SG position, a subfigure with different color levels are shown.. (For interpretation of the references to color in this figure legend, the reader is referred to the web version of this article.)

sation with NBP extend more upstream. In addition, for both NBP and RNBP, the maximum nucleation, condensation, and oxidation rates locate at the flame centerline while surface growth peaks at the flame wing. Although the surface growth and condensation rates predicted by RNBP are at the same order of magnitude (both are dominant over nucleation), the oxidation at the leaner position (i.e., downstream) compensate the condensation, such that surface growth dominates at the flame wing and finally result in the peak soot volume fraction at the flame wing (see Fig. 14(b)).

For a better illustration, we plot the source terms as functions of mixture fraction at the flame centerline in Fig. 17. It is seen that the condensation at 0.33 < Z < 0.42 by NBP, where the condensation by RNBP is nearly zero, is majorly contributed by GP1 (CV1 \rightarrow C₉H₈ \rightarrow C₉H₇ \rightarrow A2 \rightarrow soot) and GP2 (CV1 \rightarrow A1C₂H₂ \rightarrow A1C₂H \rightarrow A2C₂H₂A \rightarrow A2R5 \rightarrow soot) in Fig. 7 (the green and blue region, respectively). It is then clear that the discrepancies caused by mechanism reduction is the improper deletion of some significant species, which contributes significantly to

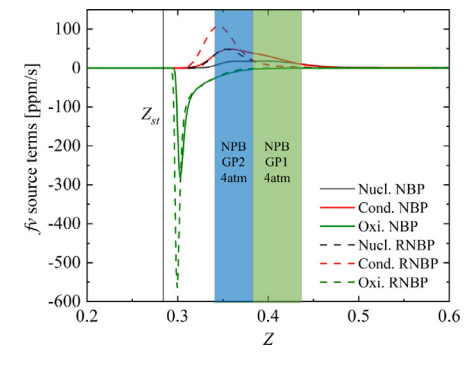


Fig. 17. The soot source terms, including nucleation, condensation and oxidation at the flame centerline as a function of mixture fraction (*Z*). NPB-GP2-4atm and NBP-GP1-4atm indicate that the highlighted mixture fraction ranges are dominated by the GPs of GP1 and GP2 in Fig. 7 (**GP1**: $C_2H_4 \rightarrow C_2H_3 \rightarrow C_2H_2 \rightarrow C_9H_8 \rightarrow C_9H_7 \rightarrow A2 \rightarrow soot;$ **GP2**: $C_2H_4 \rightarrow C_2H_3 \rightarrow C_2H_2 \rightarrow A1C_2H_2 \rightarrow A1C_2H \rightarrow A1C_2HY \rightarrow A2-A2C_2H_2A \rightarrow A2R5 \rightarrow soot).$

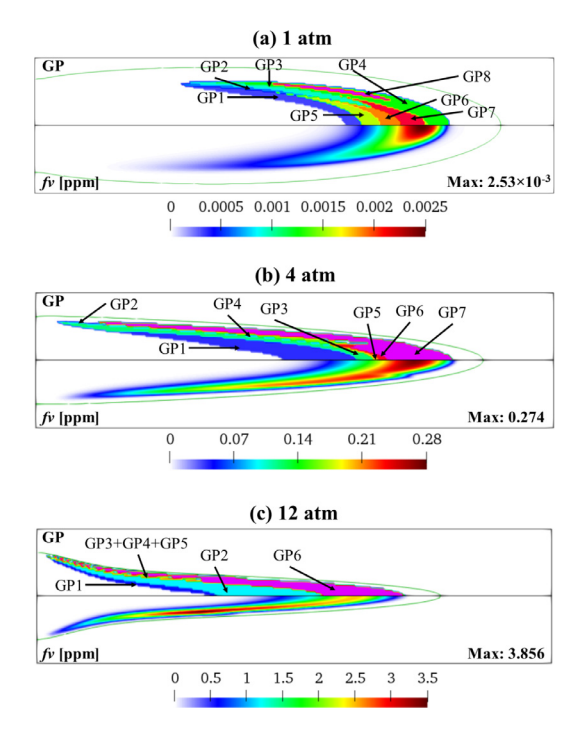


Fig. 18. The dominant GPs from fuel (i.e. C_2H_4) to soot at different spatial positions at (a) 1 atm, (b) 4 atm and (c) 12 atm, calculated with the RKAUST mechanism. The GPs details are shown in Table 3. Soot volume fraction field with the maximum soot volume fraction are also shown in the figure. As a comparison, the experimental peak soot volume fractions are 1.49 ppm and 16.8 ppm at 4 and 12 atm, respectively. The olive green solid line indicates the stoichiometric mixture fraction location. (For interpretation of the references to colour in this figure legend, the reader is referred to the web version of this article.)

the carbon flux for soot formation at 0.33 < Z < 0.42. From GP1 and GP2 in Fig. 7, we then know that C_9H_7 , C_9H_8 and A2R5 are the missing species in RNBP, which play significant roles for nucleation and condensation at 0.33 < Z < 0.42 in NBP.

To sum up, although the reduced mechanism well capture the maximum volume fraction, it showed very different soot spatial distribution and tends to give higher soot formation on the wing with increasing pressure. The important species C_9H_7 , C_9H_8 and A2R5 are missing in RNBP, leading to the under-predicted nucleation and condensation at 0.33 < Z < 0.42. Using only A2 as the precursor for dimerization could thus lead to large error. Our future work could apply SGPA as an automatic mechanism reduction tool for soot-related mechanisms, which could retain the important species in the GPs from fuel to soot but minimize the mechanism sizes.

3.4. Effect of PAH species with higher aromatic rings

In this section, the reduced KAUST (RKAUST) mechanism, with heavier PAH precursors for dimerization (i.e., BAPYR, BEPYREN, BGHIPER, ANTHAN and CORONEN), is examined. As stated in Ref. [39], the heavier PAH species significantly affect the soot volume fraction prediction. In this study, we employ SGPA method to study how these heavier PAH species influence the soot evolution in pressurized flames. The 1 atm, 4 atm and 12 atm soot field prediction together with their spatial GPs distribution are given in Fig. 18, where the maximum soot volume fraction is also indicated. Overall, the soot field is well captured by RKAUST and the maximum soot volume fractions are also in good agreement with the experimental data. Note that due to the existence of C₉H₇, C₉H₈ and A2R5 in RKAUST, the maximum soot volume fraction positions at 4 atm is well reproduced. In fact, the centerline upstream re-

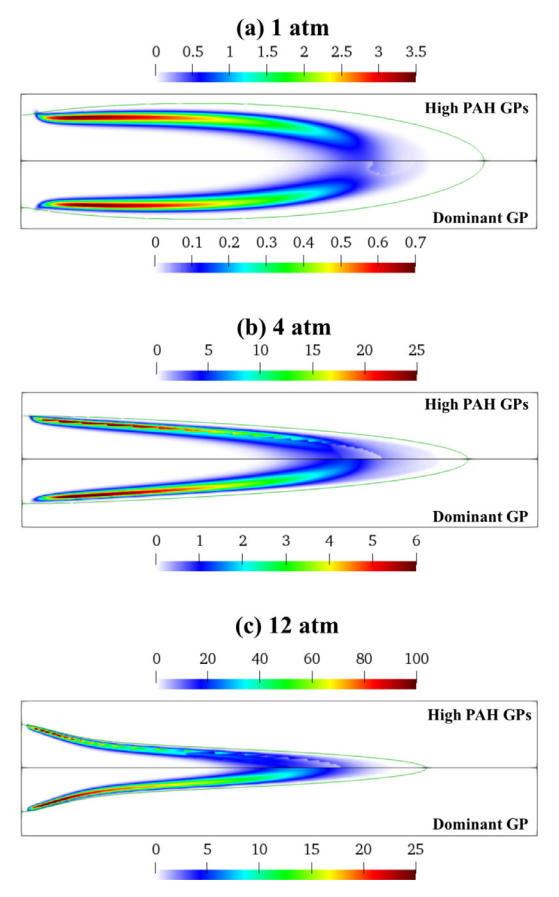


Fig. 19. Comparisons between the combined dominance of GPs that involve PAH species with high aromatic rings (High PAH GPs) and the dominance of the most dominant (Dominant GP) at (a) 1 atm, (b) 4 atm and (c) 12 atm. The most dominant GPs are GP4 at 1 atm (**GP4**: $C_2H_4 \rightarrow C_2H_3 \rightarrow C_2H_2 \rightarrow A3-4 \rightarrow A2R5- \rightarrow A2R5 \rightarrow$ soot), GP7 at 4 atm (**GP7**: $C_2H_4 \rightarrow C_2H_3 \rightarrow C_2H_2 \rightarrow$ soot) and GP 6 at 12 atm (**GP6**: $C_2H_4 \rightarrow C_2H_3 \rightarrow C_2H_2 \rightarrow$ soot). The GPs involving PAH species with higher rings at different pressures are listed in Table 4, 5 and 6. The olive green solid line indicates the stoichiometric mixture fraction location. (For interpretation of the references to colour in this figure legend, the reader is referred to the web version of this article.)

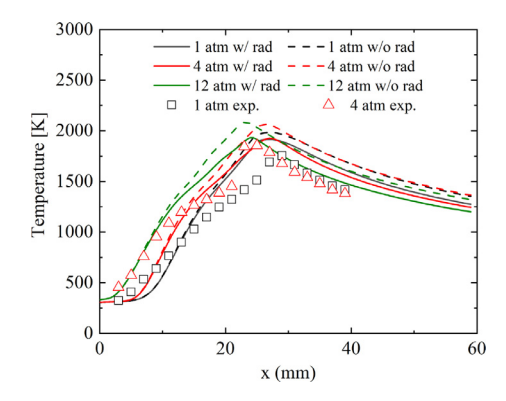


Fig. 20. Temperature profiles as a function of distance to fuel nozzle (x) at different 1, 4 and 12 atm, calculated with and without radiation. Available experimental data [6-8] at 1 and 4 atm are also shown.

gions are dominated by the GPs with C_9H_7 , C_9H_8 and A2R5, which is inline with our conclusions in the previous section.

To study the roles of the PAH species with higher rings playing in the soot evolution, we identified the GPs that pass through those PAH species with higher rings than A4 at the high soot volume fraction regions, which are all listed in Table 4–6. Although not shown in this study, their separate dominance values for these

Table 3 GPs identified by SGPA for RKAUST at different spatial locations at 1, 4 and 12 atm (see Fig. 18), $C_2H_4 \rightarrow C_2H_3 \rightarrow C_2H_2$ is lumped as CV1.

```
1 atm
                             \textbf{GP1:} \ CV1 \ \rightarrow \ C_9H_8 \ \rightarrow \ C_9H_7 \ \rightarrow \ A2R5 \ \rightarrow \ soot
                             \textbf{GP2:} \ \text{CV1} \rightarrow \text{A1} \rightarrow \text{A1-} \rightarrow \text{A1C}_2\text{H} \rightarrow \text{A1C}_2\text{H}^* \rightarrow \text{A1C}_4\text{H}_3 \rightarrow \text{A1C}_4\text{H}_3\text{u} \rightarrow \text{A2-1} \rightarrow \text{A2C}_2\text{H}_2 \rightarrow \text{A2R5} \rightarrow \text{soot}
                             \textbf{GP3:} \ \text{CV1} \rightarrow \text{C}_3\text{H}_3 \rightarrow \text{A1} \rightarrow \text{A1-} \rightarrow \text{A1C}_2\text{H} \rightarrow \text{A1C}_2\text{H}^* \rightarrow \text{A1C}_4\text{H}_3 \rightarrow \text{A1C}_4\text{H}_3\text{u} \rightarrow \text{A2-1} \rightarrow \text{A2C}_2\text{H}_2 \rightarrow \text{A2R5} \rightarrow \text{soot}
                             GP4: CV1 \rightarrow A3-4 \rightarrow A2R5- \rightarrow A2R5 \rightarrow soot
                             \textbf{GP5:} \ CV1 \ \rightarrow \ C_3H_3 \ \rightarrow \ A2R5 \ \rightarrow \ soot
                             GP6: CV1 \rightarrow C<sub>3</sub>H<sub>3</sub> \rightarrow A1- \rightarrow A1C<sub>2</sub>H \rightarrow A1C<sub>2</sub>H* \rightarrow A1C<sub>4</sub>H<sub>3</sub> \rightarrow A1C<sub>4</sub>H<sub>3</sub>u \rightarrow A2-1 \rightarrow A2C<sub>2</sub>H<sub>2</sub> \rightarrow A2R5 \rightarrow soot
                             GP7: CV1 \rightarrow A1C<sub>4</sub>H<sub>3</sub> \rightarrow A1C<sub>4</sub>H<sub>3</sub>u \rightarrow A2-1 \rightarrow A2C<sub>2</sub>H<sub>2</sub> \rightarrow A2R5 \rightarrow soot
                             GP8: CV1 \rightarrow soot
                            \textbf{GP1:} \ CV1 \ \rightarrow \ C_9H_8 \ \rightarrow \ C_9H_7 \ \rightarrow \ A4 \ \rightarrow \ soot
4 atm
                             \textbf{GP2:} \ CV1 \ \rightarrow \ C_3H_3 \ \rightarrow \ A2R5 \ \rightarrow \ soot
                             GP3: CV1 \rightarrow C<sub>9</sub>H<sub>8</sub> \rightarrow C<sub>9</sub>H<sub>7</sub> \rightarrow A2R5 \rightarrow soot
                             \textbf{GP4:} \ CV1 \rightarrow C_3H_3 \rightarrow A1\text{-} \rightarrow A1C_2H \rightarrow A1C_2H^* \rightarrow A1C_4H_3 \rightarrow A1C_4H_3u \rightarrow A2\text{-}1 \rightarrow A2C_2H_2 \rightarrow A2R5 \rightarrow sooten
                             GP5: CV1 \rightarrow C3H4-P \rightarrow C<sub>3</sub>H<sub>3</sub> \rightarrow A2R5 \rightarrow soot
                             \textbf{GP6:} \ \text{CV1} \rightarrow \text{C3H4-P} \rightarrow \text{C}_3\text{H}_3 \rightarrow \text{A1-} \rightarrow \text{A1C}_2\text{H} \rightarrow \text{A1C}_2\text{H}^* \rightarrow \text{A1C}_4\text{H}_3 \rightarrow \text{A1C}_4\text{H}_3\text{u} \rightarrow \text{A2-1} \rightarrow \text{A2C}_2\text{H}_2 \rightarrow \text{A2R5} \rightarrow \text{soot}
                             GP7: C_2H_4 \rightarrow C_2H_3 \rightarrow C_2H_2 \rightarrow soot
                            \textbf{GP1:} \ \text{CV1} \ \rightarrow \ \text{A1CH}_2 \ \rightarrow \ \text{C}_9 \text{H}_8 \ \rightarrow \ \text{C}_9 \text{H}_7 \ \rightarrow \ \text{A4} \ \rightarrow \ \text{soot}
12 atm
                             GP2: CV1 \rightarrow C<sub>9</sub>H<sub>8</sub> \rightarrow C<sub>9</sub>H<sub>7</sub> \rightarrow A4 \rightarrow soot
                             \textbf{GP3:} \ \text{CV1} \rightarrow \text{C}_3\text{H}_3 \rightarrow \text{A1-} \rightarrow \text{A1C}_2\text{H} \rightarrow \text{A1C}_2\text{H}^* \rightarrow \text{A1C}_4\text{H}_3 \rightarrow \text{A1C}_4\text{H}_3 u \rightarrow \text{A2-1} \rightarrow \text{A2C}_2\text{H}_2 \rightarrow \text{A2R5} \rightarrow \text{soot}
                             GP4: CV1 \rightarrow C<sub>3</sub>H<sub>3</sub> \rightarrow A2R5 \rightarrow soot
                             \textbf{GP5:} \ CV1 \ \rightarrow \ C_9H_8 \ \rightarrow \ C_9H_7 \ \rightarrow \ A2R5 \ \rightarrow \ soot
                             GP6: CV1 \rightarrow soot
```

Table 4Important GPs with higher aromatic ring PAH species at 1 atm.

```
C_2H_4 \rightarrow C_2H_3 \rightarrow C_2H_2 \rightarrow ANTHAN \rightarrow soot
2
                                                                \mathsf{C_2H_4} \rightarrow \mathsf{C_2H_3} \rightarrow \mathsf{C_2H_2} \rightarrow \mathsf{A3\text{-}4} \rightarrow \mathsf{A4} \rightarrow \mathsf{A4} \rightarrow \mathsf{A4} \rightarrow \mathsf{PYC2H\text{-}4} \rightarrow \mathsf{PYC2H\text{-}4JS} \rightarrow \mathsf{BEPYRENJ} \rightarrow \mathsf{BGHIPER} \rightarrow \mathsf{soot}
 3
                                                                C_2H_4 \rightarrow C_2H_3 \rightarrow C_2H_2 \rightarrow BAPYRJS \rightarrow BAPYR \rightarrow soot
                                                               C_2H_4 \rightarrow C_2H_3 \rightarrow C_2H_2 \rightarrow A3-4 \rightarrow A4 \rightarrow A4-4 \rightarrow PYC2H-4 \rightarrow PYC2H4|S \rightarrow BEPYREN| \rightarrow BGHIPE|S \rightarrow CORONEN \rightarrow soot
   4
   5
                                                               C_2H_4 \rightarrow C_2H_3 \rightarrow C_2H_2 \rightarrow A3\text{-}4 \rightarrow A4 \rightarrow A4\text{-}4 \rightarrow PYC2H\text{-}4 \rightarrow PYC2H\text{-}JS \rightarrow BEPYRENJ \rightarrow BEPYRENJ \rightarrow SOOTMAN \rightarrow SOO
   6
                                                                C_2H_4 \rightarrow C_2H_3 \rightarrow C_2H_2 \rightarrow ANTHAN \rightarrow BAPYRJS \rightarrow BAPYR \rightarrow soot
   7
                                                               C_2H_4 \rightarrow C_2H_3 \rightarrow C_2H_2 \rightarrow BAPYRJS \rightarrow ANTHAN \rightarrow soot
   8
                                                               C_2H_4 \rightarrow C_2H_3 \rightarrow C_2H_2 \rightarrow CORONEN \rightarrow soot
                                                               C_2H_4 \,\rightarrow\, C_2H_3 \,\rightarrow\, C_2H_2 \,\rightarrow\, BGHIPER \,\rightarrow\, soot
   9
                                                                C_2H_4 \,\rightarrow\, C_2H_3 \,\rightarrow\, C_2H_2 \,\rightarrow\, BGHIPER \,\rightarrow\, BGHIPEJS \,\rightarrow\, CORONEN \,\rightarrow\, soot
    10
                                                               C_2H_4 \rightarrow C_2H_3 \rightarrow C_2H_2 \rightarrow ANTHAN \rightarrow BAPYR|S \rightarrow BAPYR \rightarrow PYC2H-2 \rightarrow A4-2 \rightarrow A4 \rightarrow A4-4 \rightarrow PYC2H-4 \rightarrow PYC2H4|S \rightarrow BEPYREN| \rightarrow BGHIPER
                                                                                \rightarrow BGHIPEJS \rightarrow CORONEN \rightarrow soot
```

Table 5Important GPs with higher aromatic ring PAH species at 4 atm.

```
\mathsf{C_2H_4} \to \mathsf{C_2H_3} \to \mathsf{C_2H_2} \to \mathsf{A3\text{-}4} \to \mathsf{A4} \to \mathsf{A4\text{-}4} \to \mathsf{PYC2H\text{-}4} \to \mathsf{PYC2H\text{-}4JS} \to \mathsf{BEPYRENJ} \to \mathsf{BEPYRENJ} \to \mathsf{SOOT} \to \mathsf{BEPYRENJ} 
                                                                         C_2H_4 \rightarrow C_2H_3 \rightarrow C_2H_2 \rightarrow A3\text{-}4 \rightarrow A4 \rightarrow A4\text{-}4 \rightarrow PYC2H\text{-}4 \rightarrow PYC2H\text{-}4]S \rightarrow BEPYRENJ \rightarrow BGHIPEJS \rightarrow CORONEN \rightarrow soot \rightarrow 
                                                                         C_2H_4 \rightarrow C_2H_3 \rightarrow C_2H_2 \rightarrow A3\text{-}4 \rightarrow A4 \rightarrow A4\text{-}4 \rightarrow PYC2H\text{-}4 \rightarrow PYC2H\text{-}4|S \rightarrow BEPYRENJ \rightarrow BGHIPER \rightarrow soot
3
                                                                         C_2H_4 \rightarrow C_2H_3 \rightarrow C_2H_2 \rightarrow \text{ANTHAN} \rightarrow \text{BAPYRJS} \rightarrow \text{BAPYR} \rightarrow \text{PYC2H-2} \rightarrow \text{A4-2} \rightarrow \text{A4} \rightarrow \text{A4-4} \rightarrow \text{PYC2H-4} \rightarrow \text{PYC2H4JS} \rightarrow \text{BEPYRENJ} \rightarrow \text{BEPYREN} \rightarrow \text{soot}
                                                                         C_2H_4 \rightarrow C_2H_3 \rightarrow C_2H_2 \rightarrow ANTHAN \rightarrow BAPYRJS \rightarrow BAPYR \rightarrow soot
                                                                         C_2H_4 \,\rightarrow\, C_2H_3 \,\rightarrow\, C_2H_2 \,\rightarrow\, \text{ANTHAN} \,\rightarrow\, \text{soot}
                                                                         \mathsf{C_2H_4} \to \mathsf{C_2H_3} \to \mathsf{C_2H_2} \to \mathsf{BAPYRJS} \to \mathsf{BAPYR} \to \mathsf{soot}
                                                                         C_2H_4 \rightarrow C_2H_3 \rightarrow C_2H_2 \rightarrow BEPYRENJ \rightarrow BEPYREN \rightarrow soot
                                                                         C_2H_4 \,\rightarrow\, C_2H_3 \,\rightarrow\, C_2H_2 \,\rightarrow\, BGHIPER \,\rightarrow\, soot
                                                                      C_2H_4 \rightarrow C_2H_3 \rightarrow C_2H_2 \rightarrow C9H8 \rightarrow C9H7 \rightarrow A4 \rightarrow A4\text{--}1 \rightarrow BAPYR \rightarrow soot
  10
                                                                      C_2H_4 \rightarrow C_2H_3 \rightarrow C_2H_2 \rightarrow C9H8 \rightarrow C9H7 \rightarrow A4 \rightarrow A4-2 \rightarrow PYC2H-2 \rightarrow PYC2H2|S \rightarrow BAPYR|S \rightarrow ANTHAN \rightarrow soot
  11
                                                                      C_2H_4 \rightarrow C_2H_3 \rightarrow C_2H_2 \rightarrow C9H8 \rightarrow C9H7 \rightarrow A4 \rightarrow A4-2 \rightarrow PYC2H-2 \rightarrow PYC2H2JS \rightarrow BAPYRJS \rightarrow BAPYR \rightarrow soot
  12
  13
                                                                      C_2H_4 \rightarrow C_2H_3 \rightarrow C_2H_2 \rightarrow C9H8 \rightarrow C9H7 \rightarrow A4 \rightarrow A4\text{--}4 \rightarrow BEPYREN \rightarrow soot
                                                                         \mathsf{C_2H_4} \rightarrow \mathsf{C_2H_3} \rightarrow \mathsf{C_2H_2} \rightarrow \mathsf{C9H8} \rightarrow \mathsf{C9H7} \rightarrow \mathsf{A4} \rightarrow \mathsf{A4-4} \rightarrow \mathsf{PYC2H-4} \rightarrow \mathsf{PYC2H4JS} \rightarrow \mathsf{BEPYRENJ} \rightarrow \mathsf{BEPYRENJ} \rightarrow \mathsf{SOOT} \rightarrow \mathsf{BEPYRENJ} \rightarrow \mathsf
  15
                                                                      C_2H_4 \rightarrow C_2H_3 \rightarrow C_2H_2 \rightarrow C9H8 \rightarrow C9H7 \rightarrow A4 \rightarrow A4 \rightarrow A4 - 4 \rightarrow PYC2H - 4 \rightarrow PYC2
                                                                      C_2H_4 \rightarrow C_2H_3 \rightarrow C_2H_2 \rightarrow C9H8 \rightarrow C9H7 \rightarrow A4 \rightarrow A4-4 \rightarrow PYC2H-4 \rightarrow PYC2H4JS \rightarrow BEPYRENJ \rightarrow BEPYRER \rightarrow soot
  16
                                                                      C_2H_4 \,\rightarrow\, C_2H_3 \,\rightarrow\, C_2H_2 \,\rightarrow\, CORONEN \,\rightarrow\, soot
  17
```

Table 6Important GPs with higher aromatic ring PAH species at 12 atm.

```
C_2H_4 \rightarrow C_2H_3 \rightarrow C_2H_2 \rightarrow ANTHAN \rightarrow BAPYR | S \rightarrow BAPYR \rightarrow soot
                                     C_2H_4 \,\rightarrow\, C_2H_3 \,\rightarrow\, C_2H_2 \,\rightarrow\, ANTHAN \,\rightarrow\, soot
3
                                     C_2H_4 \,\rightarrow\, C_2H_3 \,\rightarrow\, C_2H_2 \,\rightarrow\, BAPYRJS \,\rightarrow\, ANTHAN \,\rightarrow\, soot
                                     C_2H_4 \rightarrow C_2H_3 \rightarrow C_2H_2 \rightarrow BAPYRJS \rightarrow BAPYR \rightarrow soot
                                     C_2H_4 \,\rightarrow\, C_2H_3 \,\rightarrow\, C_2H_2 \,\rightarrow\, BAPYRJS \,\rightarrow\, BEPYREN \,\rightarrow\, soot
                                     C_2H_4 \rightarrow C_2H_3 \rightarrow C_2H_2 \rightarrow BGHIPER \rightarrow soot
                                     C_2H_4 \rightarrow C_2H_3 \rightarrow C_2H_2 \rightarrow C_9H_8 \rightarrow C_9H_7 \rightarrow A4 \rightarrow A4\text{--}1 \rightarrow BAPYR \rightarrow soot
                                     \mathsf{C_2H_4} \rightarrow \mathsf{C_2H_3} \rightarrow \mathsf{C_2H_2} \rightarrow \mathsf{C_9H_8} \rightarrow \mathsf{C_9H_7} \rightarrow \mathsf{A4} \rightarrow \mathsf{A4-2} \rightarrow \mathsf{PYC2H-2} \rightarrow \mathsf{PYC2H2JS} \rightarrow \mathsf{BAPYRJS} \rightarrow \mathsf{ANTHAN} \rightarrow \mathsf{soot}
                                     C_2H_4 \rightarrow C_2H_3 \rightarrow C_2H_2 \rightarrow C_9H_8 \rightarrow C_9H_7 \rightarrow A4 \rightarrow A4-2 \rightarrow PYC2H-2 \rightarrow PYC2H2JS \rightarrow BAPYRJS \rightarrow BAPYR \rightarrow soots
 10
                                   C_2H_4 \rightarrow C_2H_3 \rightarrow C_2H_2 \rightarrow C_9H_8 \rightarrow C_9H_7 \rightarrow A4 \rightarrow A4\text{--}4 \rightarrow BEPYREN \rightarrow soot
                                     \mathsf{C_2H_4} \rightarrow \mathsf{C_2H_3} \rightarrow \mathsf{C_2H_2} \rightarrow \mathsf{C_9H_8} \rightarrow \mathsf{C_9H_7} \rightarrow \mathsf{A4} \rightarrow \mathsf{A4-4} \rightarrow \mathsf{PYC2H-4} \rightarrow \mathsf{PYC2H4JS} \rightarrow \mathsf{BEPYRENJ} \rightarrow \mathsf{BEPYREN} \rightarrow \mathsf{soot}
 11
                                   C_2H_4 \rightarrow C_2H_3 \rightarrow C_2H_2 \rightarrow C_9H_8 \rightarrow C_9H_7 \rightarrow A4 \rightarrow A4 - 4 \rightarrow PYC2H - 4 \rightarrow PYC2H
 12
                                  \begin{array}{c} C_2H_4 \rightarrow C_2H_3 \rightarrow C_2H_2 \rightarrow C_9H_8 \rightarrow C_9H_7 \rightarrow A4 \rightarrow soot \\ C_2H_4 \rightarrow C_2H_3 \rightarrow C_2H_2 \rightarrow CORONEN \rightarrow soot \end{array}
 13
14
```

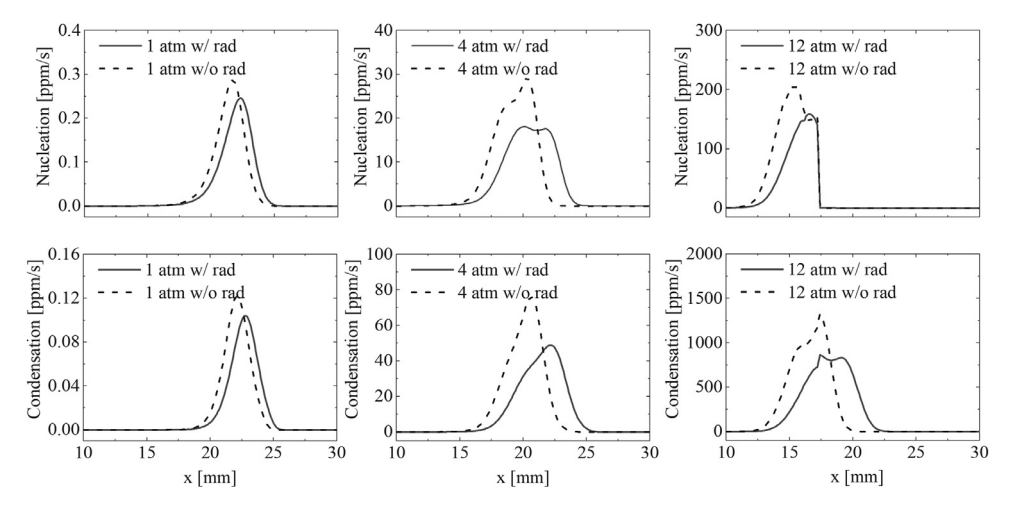


Fig. 21. Soot volume fraction nucleation and condensation rates at 1, 4 and 12 atm, calculated with and without radiation.

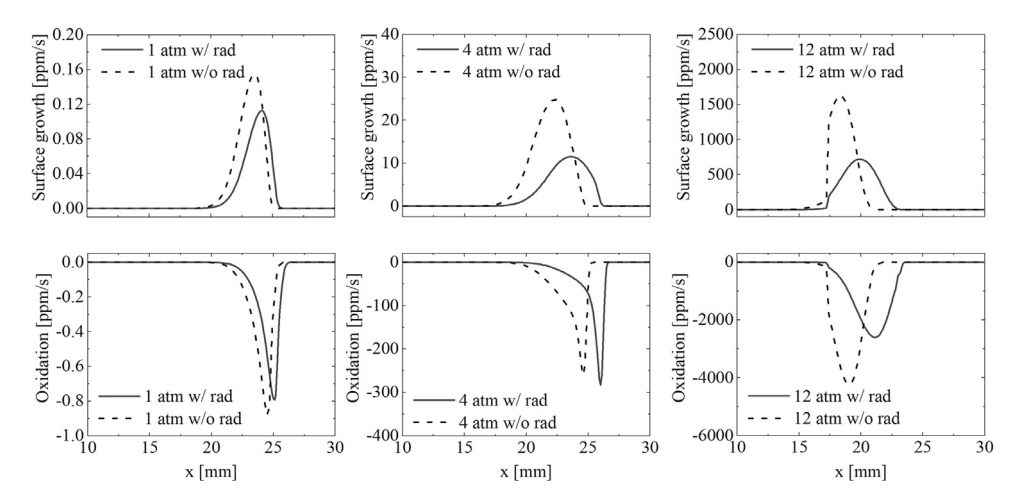


Fig. 22. Soot volume fraction surface growth and oxidation rates at 1, 4 and 12 atm, calculated with and without radiation.

GPs are low, indicating that the stand-alone contribution of these species to soot nucleation/condensation are not significant. Their dominance values calculated with Eq. (21) are summed up for these GPs and are shown in Fig. 19. Their counterparts of the most dominant GP at the similar positions (i.e., GP4 at 1 atm, GP7 at 4 atm and GP6 at 12 atm) are also calculated and shown in Fig. 19. As clearly seen from Fig. 19, although these GPs passing through PAH species with higher rings is not dominant at a certain region, the sum of the higher PAH GPs is with greater values, implying the combined important contribution of these PAH species with higher rings. It is also noted that these higher aromatic ring PAH species are mainly formed through $\rm C_2H_2$, and contribute significantly to the soot formation at the flame wing. The increasing pressure does not alter the significance of these species in soot evolution.

3.5. Effect of radiation

Note that all the results before this section consider the radiation effect. In this section, the effects of radiation on soot formation and evolution are discussed, via turning off the radiation. The temperature along the flame centerline is shown in Fig. 20. The radiation significantly reduce the temperature especially at the positions with high soot volume fraction. Though not shown here, the radiation from the greenhouse gas-phase species only induce negligible temperature drop, indicating that soot radiation is playing the dominant role. The temperature measured in the

experiment for 1 atm and 4 atm cases are also shown here. A good agreement is achieved, compared with the experimental data.

The soot source terms at 1, 4 and 12 atm along the flame centerline are shown in Figs. 21, 22. We can see that at 1 atm, the influence of radiation on the soot source terms is rather minor, because of the low soot volume fraction f_V and thus the trivial radiative heat loss at 1 atm. In contrast, when the pressure increases to 4 and 12 atm, the soot formation rates are all weakened by radiation (see Figs. 21,22). At elevated pressures, the increased soot yield enhances the radiative heat loss and thus reduces the temperature in the flame, leading to the reduced soot formation rates.

4. Conclusion

In this study, a series of ethylene-air co-flow diffusion sooting flames are simulated to study the soot formation and evolution at elevated pressures. The soot evolution is modeled by the bivariate Hybrid Method of Moments (HMOM). The simulation data of the maximum soot volume fraction and PAH species are in good agreement with the measured values, although increasing discrepancies are observed with increasing pressure.

A soot-based global pathway analysis (SGPA) method is developed to identify the pressure effects on the chemistry kinetics of soot and PAH formation. In SGPA, the carbon element flux graph from fuel to soot are directly constructed by considering one of the PAH precursors or C_2H_2 with the largest carbon flux to soot as the hub species. The pathways with carbon flux from fuel to hub

species and from hub species to soot then form the global pathways (GPs) that control the kinetics of PAH and soot formation and evolution. In this way, the most dominant GP controlling the carbon flux from fuel to soot can be selected to automatically extract valuable chemical kinetic information in multi-dimensional complex sooting reacting systems with detailed chemistry. In addition, SGPA is also able to identify the GPs controlling PAH and soot formation without missing key species in the GPs due to neglecting single species with small flux (such as DRGEP algorithms).

With the newly developed SGPA, it is seen that the dominant chemical GP is able to correctly reflect the soot evolution and formation regions. With these identified GPs, the pressure effects on the chemical kinetics of PAH and soot formation are revealed. The major findings include:

- 1. The increasing pressure shifts the first ring PAH formation from C_3H_3 recombination to the reactions of C_2H_2 . At 1 atm, the PAH growth from benzene to naphthalene is dominated by the reactions through the formation of indene (C_9H_8) and its reaction with C_3H_3 . At elevated pressures (4 and 12 atm), this growth process is dominated by the reaction of indene with C_2H_2 .
- 2. Nucleation and condensation at the very fuel rich regions are controlled by the reactions related to C₉H₇, C₉H₈ and A2R5. At 1 and 4 atm, the outer flame wing is only controlled by surface growth, while at 12 atm, the condensation GP with large dominance values at the outer flame wing indicates that condensation also becomes significant at the outer flame wing.
- 3. At 1 atm, the soot surface growth by C_2H_2 is only controlled by the H abstraction of C_2H_4 and C_2H_3 . With the increased pressures, it is found that other GPs become significant to produce C_2H_2 for soot surface growth at the flame wing, due to the third body reaction $C_2H_3 + H + M = C_2H_4 + M$.
- 4. The over-predicted C_2H_2 and A1 and under-predicted A2 and A3mole concentrations at elevated pressure are mainly due to the uncertainty of the reaction rate constants of C_2H_2 + A1CH₂ = C_9H_8 + H.
- 5. Mechanism reduction (e.g., DRGEP) without considering the global carbon flux improperly deletes several important species such as C₉H₇ and C₉H₈, which incurs incorrect soot spatial distribution at higher pressures compared with the experimental and predictions from the detailed mechanism. The SGPA method could be developed into an automatic mechanism reduction tool for chemical mechanisms with soot considerations in future work.
- 6. The PAH with high aromatic rings (e.g., A4-A7) are important in sooting flames, especially at the flame wing regions in co-flow diffusion flames. Increasing pressure does not alter the significance of the combined effects of those PAH species with high aromatic rings.
- 7. Radiation tangibly reduces the flame temperature and thus changes the soot source terms at elevated pressures, due to the higher soot yield and its caused higher radiative heat loss.

Declaration of Competing Interest

The authors declare that they have no known competing financial interests or personal relationships that could have appeared to influence the work reported in this paper.

Acknowledgments

S. Yang gratefully acknowledges the faculty start-up funding from the University of Minnesota and the grant support from NSF CBET 2038173. The authors gratefully acknowledge Prof. Graham V. Candler and the Minnesota Supercomputing Institute (MSI) for the computational resources. The helpful discussions with Dr. Junjun Guo are very much appreciated.

References

- [1] A.E. Karataş, Ö.L. Gülder, Soot formation in high pressure laminar diffusion flames, Prog. Energy Combust. Sci. 38 (6) (2012) 818–845.
- [2] L. McCrain, W.L. Roberts, Measurements of the soot volume field in laminar diffusion flames at elevated pressures, Combust. Flame 140 (1–2) (2005) 60, 60.
- [3] H.I. Joo, Ö.L. Gülder, Soot formation and temperature structure in small methane-oxygen diffusion flames at subcritical and supercritical pressures, Combust. Flame 157 (6) (2010) 1194–1201.
- [4] D.S. Bento, K.A. Thomson, Ö.L. Gülder, Soot formation and temperature field structure in laminar propane–air diffusion flames at elevated pressures, Combust. Flame 145 (4) (2006) 765–778.
- [5] P.M. Mandatori, Ö.L. Gülder, Soot formation in laminar ethane diffusion flames at pressures from 0.2 to 3.3 mpa, Proc. Combust. Inst. 33 (1) (2011) 577–584.
- [6] R.K.A. Kailasanathan, T.L. Yelverton, T. Fang, W.L. Roberts, Effect of diluents on soot precursor formation and temperature in ethylene laminar diffusion flames, Combust. Flame 160 (3) (2013) 656–670.
- [7] R.K.A. Kailasanathan, E.K. Book, T. Fang, W.L. Roberts, Hydrocarbon species concentrations in nitrogen diluted ethylene-air laminar jet diffusion flames at elevated pressures, Proc. Combust. Inst. 34 (1) (2013) 1035–1043.
- [8] S.A. Steinmetz, T. Fang, W.L. Roberts, Soot particle size measurements in ethylene diffusion flames at elevated pressures, Combust. Flame 169 (2016) 85–93.
- [9] M. Hofmann, B. Kock, T. Dreier, H. Jander, C. Schulz, Laser-induced incandescence for soot-particle sizing at elevated pressure, Appl. Phys. B 90 (3-4) (2008) 629–639.
- [10] M. Tsurikov, K.P. Geigle, V. Krüger, Y. Schneider-Kühnle, W. Stricker, R. Lückerath, R. Hadef, M. Aigner, Laser-based investigation of soot formation in laminar premixed flames at atmospheric and elevated pressures, Combust. Sci. Technol. 177 (10) (2005) 1835–1862.
- [11] N. Burali, S. Lapointe, B. Bobbitt, G. Blanquart, Y. Xuan, Assessment of the constant non-unity lewis number assumption in chemically-reacting flows, Combust. Theor. Model. 20 (4) (2016) 632–657.
- [12] A. Abdelgadir, I.A. Rakha, S.A. Steinmetz, A. Attili, F. Bisetti, W.L. Roberts, Effects of hydrodynamics and mixing on soot formation and growth in laminar coflow diffusion flames at elevated pressures, Combust. Flame 181 (2017) 39–53.
- [13] F. Liu, K.A. Thomson, H. Guo, G.J. Smallwood, Numerical and experimental study of an axisymmetric coflow laminar methane-air diffusion flame at pressures between 5 and 40 atmospheres, Combust. Flame 146 (3) (2006) 456– 471.
- [14] N.A. Eaves, A. Veshkini, C. Riese, Q. Zhang, S.B. Dworkin, M.J. Thomson, A numerical study of high pressure, laminar, sooting, ethane-air coflow diffusion flames, Combust. Flame 159 (10) (2012) 3179-3190.
- [15] N.A. Eaves, M.J. Thomson, S.B. Dworkin, The effect of conjugate heat transfer on soot formation modeling at elevated pressures, Combust. Sci. Technol. 185 (12) (2013) 1799–1819.
- [16] K.A. Thomson, Ö.L. Gülder, E.J. Weckman, R.A. Fraser, G.J. Smallwood, D.R. Snelling, Soot concentration and temperature measurements in co-annular, nonpremixed ch4/air laminar flames at pressures up to 4 mpa, Combust Flame 140 (3) (2005) 222–232.
- [17] A.E. Karataş, G. Intasopa, Ö.L. Gülder, Sooting behaviour of n-heptane laminar diffusion flames at high pressures, Combust. Flame 160 (9) (2013) 1650-1656.
- [18] E.A. Griffin, Ö.L. Gülder, Soot formation in diluted laminar ethene, propene and 1-butene diffusion flames at elevated pressures, Combust. Flame 197 (2018) 378–388
- [19] M.R. Charest, Ö.L. Gülder, C.P. Groth, Numerical and experimental study of soot formation in laminar diffusion flames burning simulated biogas fuels at elevated pressures, Combust. Flame 161 (10) (2014) 2678–2691.
- [20] J.-L. Consalvi, F. Liu, Numerical study of the effects of pressure on soot formation in laminar coflow n-heptane/air diffusion flames between 1 and 10 atm, Proc. Combust. Inst. 35 (2) (2015) 1727–1734.
- [21] G. Blanquart, P. Pepiot-Desjardins, H. Pitsch, Chemical mechanism for high temperature combustion of engine relevant fuels with emphasis on soot precursors, Combust. Flame 156 (3) (2009) 588–607.
- [22] K. Narayanaswamy, G. Blanquart, H. Pitsch, A consistent chemical mechanism for oxidation of substituted aromatic species, Combust. Flame 157 (10) (2010) 1879–1898
- [23] X. Gao, S. Yang, W. Sun, A global pathway selection algorithm for the reduction of detailed chemical kinetic mechanisms, Combust. Flame 167 (2016) 238–247.
- [24] S. Yang, X. Gao, W. Sun, Global pathway analysis of the extinction and reignition of a turbulent non-premixed flame, 53rd AIAA/SAE/ASEE Joint Propulsion Conference(2017) 4850.
- [25] X. Gao, X. Gou, W. Sun, Global pathway analysis: a hierarchical framework to understand complex chemical kinetics, Combust. Theor. Model. 23 (3) (2019) 549–571.
- [26] T. Lu, C.K. Law, A directed relation graph method for mechanism reduction, Proc. Combust. Inst. 30 (1) (2005) 1333–1341.
- [27] O. Desjardins, G. Blanquart, G. Balarac, H. Pitsch, High order conservative finite difference scheme for variable density low mach number turbulent flows, J. Comput. Phys. 227 (15) (2008) 7125–7159.
- [28] S. Dworkin, M. Smooke, V. Giovangigli, The impact of detailed multicomponent transport and thermal diffusion effects on soot formation in ethylene/air flames, Proc. Combust. Inst. 32 (1) (2009) 1165–1172.
- [29] X.-D. Liu, S. Osher, T. Chan, et al., Weighted essentially non-oscillatory schemes, J. Comput. Phys. 115 (1) (1994) 200–212.

- [30] R. Barlow, A. Karpetis, J. Frank, J.-Y. Chen, Scalar profiles and no formation in laminar opposed-flow partially premixed methane/air flames, Combust. Flame 127 (3) (2001) 2102–2118.
- [31] R.J. Hall, Radiative dissipation in planar gas-soot mixtures, J. Quant. Spectrosc. Radiat. Transfer 51 (4) (1994) 635–644.
- [32] F. Liu, H. Guo, G.J. Smallwood, Effects of radiation model on the modeling of a laminar coflow methane/air diffusion flame, Combust. Flame 138 (1–2) (2004) 136–154.
- [33] M.E. Mueller, H. Pitsch, Hybrid method of moments for modeling soot formation and growth, Combust. Flame 156 (6) (2009) 1143–1155.
 [34] S. Yang, M.E. Mueller, A multi-moment sectional method (MMSM) for track-
- [34] S. Yang, M.E. Mueller, A multi-moment sectional method (MMSM) for tracking the soot number density function, Proc. Combust. Inst. 37 (1) (2019) 1041–1048.
- [35] M.E. Mueller, G. Blanquart, H. Pitsch, A joint volume-surface model of soot aggregation with the method of moments, Proc. Combust. Inst. 32 (1) (2009) 785-792.
- [36] M.E. Mueller, G. Blanquart, H. Pitsch, Modeling the oxidation-induced fragmentation of soot aggregates in laminar flames, Proc. Combust. Inst. 33 (1) (2011) 667–674.
- [37] F. Bisetti, G. Blanquart, M.E. Mueller, H. Pitsch, On the formation and early evolution of soot in turbulent nonpremixed flames, Combust. Flame 159 (1) (2012) 317–335.
- [38] M. Frenklach, A.M. Mebel, On the mechanism of soot nucleation, Phys. Chem. Chem. Phys. 22 (9) (2020) 5314–5331.

- [39] P. Selvaraj, P.G. Arias, B.J. Lee, H.G. Im, Y. Wang, Y. Gao, S. Park, S.M. Sarathy, T. Lu, S.H. Chung, A computational study of ethylene–air sooting flames: effects of large polycyclic aromatic hydrocarbons, Combust. Flame 163 (2016) 427–436.
- [40] S. Yang, J.K. Lew, M.E. Mueller, Large eddy simulation of soot evolution in turbulent reacting flows: presumed subfilter pdf model for soot-turbulence—chemistry interactions, Combust. Flame 209 (2019) 200–213.
- [41] G. Blanquart, H. Pitsch, A joint volume-surface-hydrogen multi-variate model for soot formation, Combustion generated fine carbonaceous particles, Chapter 27, 2019, pp. 437–463.
- [42] M. Frenklach, H. Wang, Detailed modeling of soot particle nucleation and growth, Symp. (Int.) Combust. 23 (1) (1991) 1559–1566.
- [43] S.B. Dworkin, Q. Zhang, M.J. Thomson, N.A. Slavinskaya, U. Riedel, Application of an enhanced PAH growth model to soot formation in a laminar coflow ethylene/air diffusion flame, Combust. Flame 158 (9) (2011) 1682–1695.
- [44] V. Kislov, A. Mebel, The formation of naphthalene, azulene, and fulvalene from cyclic c5 species in combustion: an ab initio/RRKM study of 9-h-fulvalenyl (c5h5- c5h4) radical rearrangements, J. Phys. Chem. A 111 (38) (2007) 9532–9543.
- [45] P. Pepiot-Desjardins, H. Pitsch, An efficient error-propagation-based reduction method for large chemical kinetic mechanisms, Combust. Flame 154 (1-2) (2008) 67-81.